Full Title:

The mesodermal source of fibronectin is required for heart morphogenesis and cardiac outflow tract elongation by regulating cell shape, polarity, and mechanotransduction in the second heart field.

Short Title:

Role of mesodermal fibronectin in cardiac development

Authors:

Cecilia Arriagada and Sophie Astrof*

Affiliation:

Department of Cell Biology and Molecular Medicine, Cardiovascular Research Institute, Rutgers Biomedical and Health Sciences, 185 South Orange Ave, Newark, NJ, 07103, USA.

*Author for correspondence: Sophie Astrof, Ph.D.

Phone: 617-429-8295

E-mail: sophie.astrof@rutgers.edu

Abstract

Failure in the elongation of the cardiac outflow tract results in congenital heart disease due to ventricular septum defects and misalignment of the great vessels. The cardiac outflow tract lengthens by the accretion of progenitors derived from the second heart field (SHF). SHF cells in the splanchnic mesoderm are exquisitely regionalized and organized into an epithelial-like layer forming the dorsal pericardial wall (DPW). Tissue tension within the DPW, cell polarity and proliferation are requisite processes regulating the addition of SHF-derived cells to the heart and elongation of the cardiac outflow tract. However, genes regulating these processes are not completely understood. Using conditional mutagenesis in the mouse, we show that fibronectin (*Fn1)* synthesized by the SHF is a central regulator of the epithelial architecture in the DPW. Fn1 expression is enriched in the anterior DPW and mediates outflow tract elongation by regulating cell polarity, shape, cohesion, and mechanotransduction. Our studies establish that Fn1 synthesized specifically by the mesoderm coordinates multiple cellular behaviors in the anterior DPW requisite for the elongation of the cardiac outflow tract and embryonic viability.

Introduction

Congenital heart disease (CHD) is one of the most common birth defects. An estimated 40,000 newborns in the U.S. are affected by CHD each year (Tsao et al., 2022). Therefore, it is important to understand the cellular and molecular mechanisms regulating cardiac morphogenesis and the alterations that cause CHD. Several sources of cardiac progenitor cells have been identified (Zhang et al., 2021). Progenitors in the first heart field mainly contribute to the left ventricle, while progenitors in the second heart field (SHF) contribute to the right ventricle, the outflow tract (OFT), and the atria. Correct formation and elongation of the OFT are necessary for the proper morphogenesis of the arterial pole of the heart, e.g., for intraventricular septation and correct positioning of the great vessels relative to the cardiac chambers (Cortes et al., 2018). Defects in these processes are among the most common causes of CHD (Tsao et al., 2022). OFT forms as a single tube connecting the heart with the systemic circulation. In the mouse, the OFT elongates between embryonic day (E) 8.5 and E10.75 of development by the addition of the SHF cells to the nascent heart tube (Meilhac and Buckingham, 2018). The aberrant contribution of SHF cells to the OFT results in defective elongation of the cardiac OFT leading to aberrant septation and alignment of the arterial pole of the heart.

SHF cells in the dorsal pericardial wall (DPW) (Fig S1A), directly behind the forming heart, exhibit epithelial properties such as apicobasal polarity (Cortes et al., 2018; Francou et al., 2014). Aberrations in SHF cell polarity and cohesion in the DPW result in shortened OFT and CHD (Cortes et al., 2018; Li and Wang, 2018). For instance, *Tbx1*, a key transcription factor mutated in 22q11 deletion syndrome, mediates OFT elongation by

63 regulating SHF cell polarity, organization of the actin cytoskeleton, and epithelial tension
64 in the DPW (Francou et al., 2017; Francou et al., 2014). Similarly, mediators of non-
65 canonical Wnt signaling such as *Vngl2, Wnt5a,* and *Dvl* mediate OFT elongation by
66 regulating apicobasal polarity of SHF cells in the DPW, actin cytoskeleton, and cell
67 intercalation behaviors important for the movement of SHF cells in the DPW to join the
68 OFT (Li et al., 2019; Li et al., 2016; Li and Wang, 2018; Ramsbottom et al., 2014; Sinha
69 et al., 2015; Sinha et al., 2012).
70
71 In addition to being polarized, SHF cells in the DPW are regionalized along the anterior-
72 posterior and left-right axes (Bajolle et al., 2008; Kelly, 2023). For example, *Osr1, Hoxb1*,
73 and *Wnt5a* are expressed in the posterior DPW, while *Tbx1* is expressed in the anterior
74 (Stefanovic et al., 2020). This regionalization is important for OFT elongation and
75 morphogenesis (Li and Wang, 2018; Stefanovic et al., 2020). We noticed that the
76 expression of the extracellular matrix (ECM) glycoprotein *Fn1* was enriched in the anterior
77 DPW at the protein and *mRNA* levels. In our previous studies, we found that cardiac OFTs
78 were short in Fn1-null mutants (Mittal et al., 2013). Conditional mutagenesis indicated
79 that the expression of Fn1 and its major receptor integrin $\alpha5\beta1$ in the *Isl1* lineage was
80 required for OFT elongation (Chen et al., 2015). These experiments underscore the
81 important role of Fn1 in heart development. However, mechanisms by which Fn1
82 regulates OFT elongation have not yet been investigated.
83
84 Prior to heart formation, *Fn1* mRNA is broadly expressed in the paraxial and lateral plate
85 mesoderm of early (1-3 somite) murine embryos (Pulina et al., 2011). During heart

86 development (6-23 somites), *Fn1* mRNA continues to be expressed in the splanchnic
87 mesoderm, while its expression in differentiated cardiomyocytes is nearly lost (Mittal et
88 al., 2010). Mesodermal populations expressing *Fn1 mRNA* contain cardiac progenitors.
89 Since heart development is affected in global Fn1-null embryos and embryos with
90 conditional deletion of Fn1 in the *Isl1* lineage (Chen et al., 2015; Mittal et al., 2013), we
91 hypothesized that Fn1 synthesized by cardiac progenitors regulates heart development.
92 To investigate this hypothesis, we used the *Mesp1*$^{Cre/+}$ knock-in strain to conditionally
93 ablate Fn1 expression in the anterior mesoderm. In this manuscript, we show that
94 mesodermal Fn1 coordinates multiple cellular behaviors regulating the accretion of SHF
95 cells from the DPW during OFT elongation. The deletion of the mesodermal Fn1 results
96 in aberrant cellular architecture in the anterior DPW cells contiguous with the elongating
97 OFT. Our studies indicate that Fn1 secreted by the mesoderm mediates OFT elongation
98 by regulating cardiac progenitor cell shape, apicobasal polarity, and
99 mechanotransduction.
100

101 **Results**

102 **Mesodermal synthesis of Fn1 is required for cardiogenesis and embryonic viability.**
103 The expression of the transcription factor Mesp1 marks the earliest known cardiac
104 progenitors; descendants of Mesp1-expressing cells contribute to all mesodermally-
105 derived cells of the heart (Saga et al., 1996; Saga et al., 1999). Therefore, we used the
106 *Mesp1*$^{Cre/+}$ strain to conditionally ablate *Fn1* expression from heart precursors. Although
107 Mendelian proportions of all genotypes were recovered at E9.5, we found some Fn1$^{flox/-}$;
108 *Mesp1*$^{Cre/+}$ mutant embryos at E9.5 with mild cardiac defects (S1B-D1 Fig). However, only

109 50% of the expected number of Fn1$^{flox/-}$; *Mesp1*$^{Cre/+}$ embryos were recovered at E10.75
110 (S1E-G Fig). All the recovered mutants at E10.75 had prominent cardiac edema,
111 defective heart, and were degenerating (S1E-F1 Fig). No Fn1$^{flox/-}$; *Mesp1*$^{Cre/+}$ mutants
112 were recovered after E13.5 days of gestation (S1G Fig). These data indicated that the
113 expression of *Fn1* in the Mesp1 lineage is required for heart development and embryonic
114 viability.
115
116 **Mesodermal Fn1 regulates the elongation of the cardiac OFT.**
117 The shape of the heart in E10.75 mutants suggested that mesodermal Fn1 played a role
118 in the development of the cardiac OFT (S1E-F1 Fig). To test this hypothesis, we first
119 examined embryos at E8.5 (8-12 somites), when the OFT begins to form. At this stage of
120 development, we did not find alterations in any cardiac structures, and the nascent OFTs
121 in mutants and controls were of similar lengths (S2 Fig). The heart remained similar in
122 shape in control and mutant embryos at 18-19 somites, and the OFT length was
123 comparable among control and mutant genotypes at this stage (Fig. 1A-D). However, at
124 20-25 somites, OFT length in mutant embryos was significantly shorter than in controls,
125 and both the proximal and the distal portions of the OFT were affected at this stage (Fig.
126 1E-H). In control embryos, the right and the left ventricles align in the plane perpendicular
127 to the embryonic anterior-posterior axis (Fig. 1I). In mutants with shortened OFT, this
128 alignment is distorted and the right ventricle is shifted anteriorly due to the decreased
129 length of the OFT (Li et al., 2016). The alignment of the right ventricle is similarly distorted
130 in Fn1$^{flox/-}$; *Mesp1*$^{Cre/+}$ mutants (Fig. 1J-K). Together, these data indicate that mesodermal
131 Fn1 mediates cardiogenesis by regulating OFT elongation.

132

133 **Mesodermal Fn1 regulates the epithelial architecture of the dorsal pericardial wall.**
134 Cardiac OFT elongates through the addition of cardiac precursors from the SHF in the
135 first and second pharyngeal arches and the splanchnic mesoderm of the DPW (Cortes et
136 al., 2018; Li and Wang, 2018; Meilhac and Buckingham, 2018). The length of the OFT
137 remained comparable among controls and mutants by the ~19th somite stage of
138 development, suggesting that the addition of SHF cells from the pharyngeal arches was
139 not affected by the deletion of the mesodermal source of Fn1 (Meilhac and Buckingham,
140 2018). However, cells in the DPW of E8.5 mutants were disorganized (Fig. 2). Instead of
141 a single layer of epithelial-like cells, as seen in control Fn1$^{flox/+}$; *Mesp1*$^{Cre/+}$ embryos, cells
142 in the anterior DPW of Fn1$^{flox/-}$; *Mesp1*$^{Cre/+}$ mutants were multilayered (compare Fig. 2A-
143 A1 with Fig. 2E-E1). In controls, DPW cells appeared ellipsoid, regularly oriented along
144 the dorsal-ventral axis, and neatly stacked along the entire length of the DPW (Fig. 2A-
145 D). In the mutants, SHF cells were more spherical in the anterior DPW (Fig. 2E-H). To
146 quantify differences in cell shapes in 2D and 3D, we measured cell circularity and ellipticity
147 in controls and mutants (Fig. 2I-L). Circularity is the ratio of cell width to cell length.
148 Elongated cells have circularity indexes that deviate from 1, while cuboid or spherical cells
149 have circularity indexes close to 1. Differences in circularity indexes among SHF cells in
150 the anterior DPW were statistically significant between controls and mutants (Fig. 2I).
151 However, in the posterior DPW, the circularity of control and mutant cells were
152 comparable (Fig. 2J). To determine if 3D cell shape was also affected in the mutants, we
153 segmented individual SHF cells in the anterior DPW and measured ellipticity. Ellipticity
154 was higher in control embryos than in mutants, indicating that in the absence of

155 mesodermal Fn1, SHF cells in the anterior DPW were more spherical than in controls (Fig
156 2K). The volume of individual SHF cells was not affected in the mutants at this stage (Fig.
157 2L). These differences in 2D and 3D cell shapes were observed at E8.5 and preceded
158 the shortening of the cardiac OFT. The aberrant epithelial architecture of the anterior
159 DPW persisted at E9.5, at the time when defective OFT elongation became detectable in
160 the mutants (S3A-K Fig). In addition to altered cell shape, cell volume was also decreased
161 in E9.5 mutants (S3L Fig). Together, these data suggest that alterations in SHF cell shape
162 in the anterior DPW give rise to defective OFT elongation in the mutants.
163

164 **Mesodermal Fn1 regulates SHF cell orientation and apicobasal polarity in the**
165 **anterior DPW.**

166 To determine mechanisms by which mesodermal Fn1 regulates the cellular architecture
167 of the DPW, we tested the hypothesis that Fn1 was important for apicobasal cell polarity.
168 At E8.5, the Golgi apparatus was positioned toward the apical surface of SHF cells along
169 the entire length of the DPW (Fig. 3A-A4). In contrast, in the mutants, the orientation of
170 the Golgi apparatus was disorganized in the anterior DPW, and in some SHF cells, the
171 Golgi apparatus faced toward the basal side (Fig. 3B-B1, B3, 3C, and 3D). However, in
172 the posterior DPW, the Golgi apparatus was positioned toward the apical cell side in
173 controls and mutants alike (compare Fig. 3A2 with 3B2, quantified in Fig.3A4, B4, and
174 Fig. 3E).
175

176 Similar to disorganized Golgi orientation, markers of the apical cell surface were re-
177 distributed in the mutants and were also present at the basal surface of SHF cells in the

178 anterior DPW (Fig. 4). These proteins included podocalyxin (compare Fig. 4A1 with Fig.
179 4B1 quantified in Fig. C and Fig. 4A2 with Fig. 4B2 quantified in Fig. 4D) and atypical
180 PKC ζ (aPKC ζ) (compare Fig. 4E-F with Fig. 4H-I quantified in Fig. 4K). Basal cell
181 properties of SHF cells were not as distorted as apical in the mutants: the expression of
182 laminin γ1 was disorganized only in 1 of 3 E8.5 mutants (Fig. 4G, J) and cellular
183 protrusions on the basal side of SHF cells were present in equal numbers in controls and
184 mutants at E9.5 (S4 Fig). These studies suggest the expansion of the apical surface of
185 SHF cells in the anterior DPW, while the basal cell surface was properly specified.
186 Changes in apical cell polarity were observed at E8.5 before defects in the OFT
187 elongation were detectable; however, by E9.5, apicobasal cell polarity recovered in the
188 mutants (S5 Fig). Altogether, these data show that changes in SHF cell shape and polarity
189 within the anterior DWP preceded changes in the OFT elongation and were likely causes
190 of defective OFT elongation in the mutants (Cortes et al., 2018; Li and Wang, 2018).
191
192 **Mesodermal Fn1 regulates cell cohesion in the SHF and collective cell migration.**
193 Adherens junctions form between the apical and basal cell surfaces (Nelson, 2003).
194 Therefore, we examined the localization of N-Cadherin in the DPW and found that N-
195 cadherin levels were downregulated in the DPW of the mutants (Fig. 5A-D1). To quantify
196 these changes, we used mouse embryo fibroblasts (MEFs) as a model system and
197 generated four lines of MEFs (S6 Fig): 1) $Fn1^{flox/+}$ MEFs, in which wild-type Fn1 protein
198 can be produced from both *Fn1* alleles, 2) $Fn1^{flox/-}$ MEFs, in which wild-type Fn1 protein
199 is generated from the floxed *Fn1* allele, and "-" *Fn1* allele is a null allele, 3) $Fn1^{/+}$ MEFs,
200 in which the floxed region of *Fn1* allele was resulting in one Fn1-null allele (Δ) (Sakai et

201 al., 2001) and one wild-type *Fn1* allele in these MEFs, and 4) $Fn1^{\Delta/-}$ MEFs, which are
202 Fn1-protein-null (S6 Fig). Immunofluorescence and quantitative Western blot analyses
203 showed that total and cell-surface levels of N-Cadherin were downregulated in $Fn1^{\Delta/-}$
204 MEFs (Fig. 5E-O1). We observed similar levels of N-cadherin between $Fn1^{flox/+}$ and $Fn1^{\Delta/+}$
205 MEFs, indicating that the decrease in N-cadherin in $Fn1^{\Delta/-}$ MEFs was not due to and non-
206 specific effect of the Cre infection (Fig. 5E-G and Fig5H-O1). Cell cohesion is important
207 for the collective cell migration (Friedl and Mayor, 2017). Since N-Cadherin was
208 downregulated in $Fn1^{\Delta/-}$ MEFs (Fig. 5E-K), we used this model to determine whether the
209 synthesis of Fn1 by MEFs was important for their collective cell migration. Monolayer
210 scratch assay showed that, indeed, scratch wounds made in $Fn1^{\Delta/-}$ MEF monolayers
211 closed slower than in $Fn^{flox/+}$, $Fn^{flox/-}$, or $Fn1^{\Delta/+}$ MEFs (S7 Fig). Downregulation of N-
212 Cadherin in the cardiac progenitors within the anterior DPW causes their precautious
213 differentiation (Soh et al., 2014). Consistent with these findings, we observed an
214 expanded expression domain of the sarcomeric myosin heavy chain (assayed by the MF-
215 20 antibody) in the anterior DPW of our mutants (S8 Fig). Together, these studies suggest
216 that mesodermal Fn1 regulates cell cohesion and collective cell migration of SHF cells,
217 facilitating the maintenance of the progenitor cell state in the DPW and the cellular
218 movement from the DPW to the OFT during its elongation.
219
220 **Mesodermal Fn1 regulates mechanotransduction in the dorsal pericardial wall.**
221 Nuclear localization of YAP is regulated by the mechanical tension in the DPW and is
222 important for the proliferation of DPW cells and OFT elongation (Francou et al., 2017).
223 YAP is a central transducer of the mechanical signals (Dupont, 2016). Defective shape

224 and orientation of SHF cells in the anterior DPW of Fn1$^{flox/-}$; *Mesp1*$^{Cre/+}$ mutants suggested
225 that mutant SHF cells in the anterior DPW are deficient in generating, sensing, or
226 responding to mechanical cues. The remodeling of the actin cytoskeleton and nuclear
227 localization of YAP are known to be facilitated by cell adhesion to Fn1 *in vitro* (Kim and
228 Gumbiner, 2015; Singh et al., 2010). To test whether mesodermal Fn1 was required for
229 cytoskeletal remodeling and nuclear localization of YAP in the DPW, we first stained
230 control and Fn1$^{flox/-}$; *Mesp1*$^{Cre/+}$ mutant embryos to detect filamentous (F)-actin. We found
231 that F-actin organization at E9.5 was disrupted specifically in the anterior DPW of the
232 mutants (Fig. 6): The orientation of F-actin filaments was disorganized (Fig. 6A-J) and F-
233 actin filaments were shorter in the anterior DPW (Fig. 6K). The length and orientation of
234 F-actin in the posterior and middle DPW were comparable between genotypes (S9 Fig).
235
236 Changes in cell shape and actomyosin cytoskeleton serve are faithful readouts of altered
237 mechanical tension in epithelial tissues (Luciano et al., 2022). Cells in the anterior DPW
238 are apically constricted and have a smaller apical surface area than cells in the posterior
239 DPW (Francou et al., 2017). Consistent with these findings, we observed the enrichment
240 of F-actin and an activated form of Myosin Light Chain 2 phosphorylated on Ser19
241 (pMLC), capable of driving the actomyosin contractility (Somlyo and Somlyo, 1994) at the
242 apical cell surface of the DPW (Fig. 7A-B2, E-F2). In contrast, apical enrichment of F-
243 actin and pMLC was lost in Fn1$^{flox/-}$; *Mesp1*$^{Cre/+}$ mutants (Fig. 7, compare Fig. 7B1 with
244 7D1 and Fig. 7F1 with 7H1). These changes were concordant with decreased nuclear
245 YAP localization in the anterior DPW of mutants (Fig. 8, compare Fig. 8B1 with 8C1,

246 quantified in Fig. 8D). Nuclear localization of YAP in the posterior DPW was not affected
247 (compare Fig. 8B2 with 8C2, quantified in Fig. 8E).
248
249 Cell adhesion to Fn1 regulates the nuclear localization of YAP (Kim and Gumbiner, 2015).
250 YAP, in turn, is a central integrator of mitogenic, biomechanical, and cell polarity cues
251 important for cell proliferation (Borreguero-Munoz et al., 2019; Fan et al., 2013). Inhibition
252 of YAP causes decreased proliferation of DPW cells in developing embryos (Francou et
253 al., 2017). Consistent with these studies, cell proliferation (but not cell survival) was
254 decreased in the DPW and the heart of Fn1$^{flox/-}$; *Mesp1*$^{Cre/+}$ mutants, while the proliferation
255 of adjacent non-mesodermal tissues was not affected (Fig. 9, S10-S12 Figs). Altogether,
256 altered (more rounded) cell shape, the re-distributed of actomyosin cytoskeleton from the
257 apical surface, decreased cell volume, and decreased levels of nuclear YAP are all
258 indicators of an altered mechanical microenvironment (Perez Gonzalez et al., 2018) in
259 the anterior DPW of Fn1$^{flox/-}$; *Mesp1*$^{Cre/+}$ mutants.
260
261 **Mesodermal Fn1 is the essential source of Fn1 in the anterior DPW.**
262 We next asked whether defects observed in the DPW of Fn1$^{flox/-}$; *Mesp1*$^{Cre/+}$ mutants were
263 due to decreased levels of Fn1 or were caused by the absence of Fn1 protein made
264 specifically in the mesoderm. *Fn1 mRNA* and protein are dynamically and non-uniformly
265 expressed in developing embryos (Chen et al., 2015; Mittal et al., 2010), and previous
266 studies demonstrated cell-autonomous roles of Fn1 during embryonic development,
267 angiogenesis, and cell migration (Cseh et al., 2010; Turner et al., 2017; Wang and Astrof,
268 2016; Zimmerman et al., 2017). Cells in the DPW and the pharyngeal endoderm are

269 closely apposed in mid-gestation embryos, and *Fn1* mRNA is synthesized by both tissues
270 (Fig. 10A-B2). At E8.5, Fn1 protein is present in the DPW and the heart of controls, but
271 it is downregulated in Fn1$^{flox/-}$; *Mesp1*$^{Cre/+}$ mutants (S13A-H Fig).
272
273 Although there were no differences in Fn1 protein levels between the anterior and
274 posterior DPW in control embryos at E8.5 (the ratio of Fn1 protein in aDPW to that in
275 pDPW is close to 1, S13E Fig), at E9.5, *Fn1* mRNA was enriched nearly 2-fold in the
276 anterior DPW relative to the posterior (Fig. 10A-C). This enrichment is particularly well-
277 visualized in control Fn1$^{flox/+}$; *Mesp1*$^{Cre/+}$ embryos (Fig. 10D-F2). In these embryos, one
278 allele of Fn1 is deleted in the mesoderm, resulting in a ~50% decrease in *Fn1 mRNA* in
279 the DPW relative to the wild-type (Fig. 10G). In Fn1$^{flox/-}$; *Mesp1*$^{Cre/+}$ mutants, levels of *Fn1*
280 mRNA in the entire DPW were low (Fig. 10H-I2 and 10G, J). However, *Fn1 mRNA*
281 remained synthesized by the endoderm (Fig. 10I1-I2, yellow arrowheads). The loss of
282 *Fn1 mRNA* in the mesoderm but not in the endoderm is consistent with the known
283 specificity of Cre expression in the *Mesp1*$^{Cre/+}$ strain (Saga et al., 1996; Saga et al., 1999)
284
285 Similar to *Fn1* mRNA , Fn1 protein was also enriched in the anterior DPW relative to the
286 posterior (Fig. 10K-L). Despite the efficient downregulation of *Fn1 mRNA* in the
287 mesoderm of the DPW, *Fn1* mRNA synthesis from the endoderm resulted in a similar
288 accumulation of Fn1 protein in the anterior DPW in controls and mutants at E9.5 (Fig.
289 10M-P). Moreover, the Fn1 protein was localized between the germ layers and enriched
290 in the anterior DPW in controls and mutant alike (Fig. 10L). But despite the presence of

291 similar levels of Fn1 protein, Fn1 derived from the endoderm did not rescue defects in the
292 architecture of the DPW in the mutants.
293
294
295 To rule out the possibility that differences in Fn1 protein levels contributed to defects in
296 the DPW in Fn1$^{flox/-}$; *Mesp1*$^{Cre/+}$mutants, we deleted Fn1 using *Sox17*$^{2A\text{-}iCre/+}$ strain, in
297 which Cre recombinase is expressed in the endoderm and endothelium (Engert et al.,
298 2009). In Fn1$^{flox/-}$; *Sox17*$^{2A\text{-}iCre/+}$mutants, *Fn1 mRNA* was downregulated in the endoderm,
299 but it was still synthesized by the SHF cells of the DPW (compare S14A-A1 Fig with S14D-
300 D1 Fig). And although the levels of Fn1 protein underlying the DPW were substantially
301 reduced in Fn1$^{flox/-}$; *Sox17*$^{2A\text{-}iCre/+}$mutants (compare S14B-B1 Fig with S14E-E1 Fig), the
302 epithelial organization and the expression of N-cadherin were not as affected in Fn1$^{flox/-}$;
303 *Sox17*$^{2A\text{-}iCre/+}$mutants as they were in Fn1$^{flox/-}$; *Mesp1*$^{Cre/+}$mutants (S14C-C1, S14F-F1
304 Fig). Together, these data indicate that 1) Fn1 synthesized by the mesoderm rather than
305 total levels of Fn1 are required for the proper cellular architecture of the DPW, 2) the
306 presence of Fn1 protein synthesized by the endoderm is not sufficient to rescue the
307 absence of mesodermal Fn1, and 3) that synthesis of Fn1 by the DPW is specifically
308 required for the proper cellular architecture and mechanotransduction in the anterior DPW
309 to mediate OFT elongation, heart development, and embryonic viability (Fig. 11).
310

311 **Discussion**

312 Here we show that Fn1 synthesized by the mesoderm is required for proliferation, cell
313 shape, cell polarity, orientation, and the orderly stacking of SHF cells in the anterior DPW.

314 In Fn1$^{flox/-}$; *Mesp1*$^{Cre/+}$mutants, defects in these properties occur prior to the observable
315 deficiencies in the OFT elongation, indicating that defects in DPW architecture cause
316 aberrant OFT elongation in the absence of Fn1 synthesized by the mesoderm.
317
318 Cell adhesion to Fn1 facilitates the remodeling of the actomyosin cytoskeleton and
319 synergizes with growth factor signaling to promote the sustained activation of Erk, the
320 expression of cyclin D1, and cell cycle progression (Bohmer et al., 1996; Roovers and
321 Assoian, 2003; Walker et al., 2005). While cellular architecture was mainly affected in the
322 anterior DPW in Fn1$^{flox/-}$; *Mesp1*$^{Cre/+}$embryos, cell proliferation was affected along the
323 entire length of the DPW as well as in the heart, where the mesoderm is the sole source
324 of Fn1 protein. Therefore, it is possible that in the DPW and the heart, Fn1 regulates
325 proliferation via multiple mechanisms; in the anterior DPW, the defect in cell proliferation
326 may be secondary to changes in actomyosin cytoskeleton, cell shape, and the nuclear
327 localization of YAP, while in the posterior DPW and the heart, Fn1 may regulate
328 proliferation directly.
329
330 At the early stages of OFT formation, at E8.5, *Fn1* mRNA and protein are synthesized by
331 the pharyngeal endoderm and the DPW. At this stage, the Fn1 protein is uniformly
332 localized at the basal side along the entire length of the DPW, between the mesoderm
333 and the endoderm. Fn1 protein in this region is decreased in Fn1$^{flox/-}$; *Mesp1*$^{Cre/+}$mutants.
334 It is possible, then, that the onset of defects in cell proliferation and DPW architecture
335 results from the diminished levels of Fn1 at E8.5 and that the anterior DPW cells are
336 especially sensitive to Fn1 levels for maintaining the proper cellular architecture.

337 However, the depletion of Fn1 protein in Fn1$^{flox/-}$; *Sox17*$^{2A\text{-}iCre/+}$ mutants, where Fn1 was
338 ablated in the endoderm, was even more severe than in Fn1$^{flox/-}$; *Mesp1*$^{Cre/+}$ mutants.
339 Despite the dramatic decrease in the levels of Fn1 protein underlying the DPW in Fn1$^{flox/-}$
340 ; *Sox17*$^{2A\text{-}iCre/+}$, the cellular architecture of the DPW and the expression of N-Cadherin at
341 cell-cell junctions in Fn1$^{flox/-}$; *Sox17*$^{2A\text{-}iCre/+}$ mutants were comparable to controls. These
342 results suggest that the decrease in Fn1 levels at E8.5 cannot solely explain cellular
343 defects in the anterior DPW of Fn1$^{flox/-}$; *Mesp1*$^{Cre/+}$ mutants.
344
345 The OFT and DPW are exquisitely regionalized, with distinct genetic programs regulating
346 OFT elongation and the development of the arterial pole of the heart (Bajolle et al., 2006;
347 Bajolle et al., 2008; Kelly, 2023; Li and Wang, 2018; Rammah et al., 2022; Ramsbottom
348 et al., 2014; Stefanovic et al., 2020; Theveniau-Ruissy et al., 2008; Xia et al., 2019). We
349 found that Fn1 is an important factor in this regionalization and provided additional
350 evidence that cellular architecture along the anterior-posterior axis is differentially
351 regulated.
352
353 In the caudal portion of the DPW, actin cytoskeletal dynamics and cell intercalation are
354 regulated by non-canonical Wnt signaling mediated by *Wnt5a* and *Dvl* (Li et al., 2019; Li
355 et al., 2016; Sinha et al., 2015; Sinha et al., 2012). Cell intercalations in the posterior
356 DPW lead to the overall displacement of the DPW cells toward the anterior pole, “pushing”
357 them into the OFT, facilitating the OFT elongation (Li and Wang, 2018). In the OFT
358 immediately adjacent to the anterior DPW, *Vngl2* and *Hand2* regulate cell-cell and cell-
359 ECM interactions mediating intercellular intercalations and the lengthening of the OFT

360 (Ramsbottom et al., 2014; Xia et al., 2019). In the anterior DPW, cellular architecture is
361 regulated by *Tbx1,* where its expression is enriched (Francou et al., 2014; Stefanovic et
362 al., 2020). Deletion of *Tbx1* leads to defects in cell-extracellular matrix interactions, cell
363 shape, organization, polarity, and actin cytoskeletal dynamics (Alfano et al., 2019;
364 Francou et al., 2014), resulting in the altered tension in the DPW and defective OFT
365 elongation (Francou et al., 2017). Similar to *Tbx1*, *Fn1* mRNA synthesis and protein
366 localization are enriched in the anterior DPW at E9.5, where Fn1 regulates cell shape,
367 orientation, and biomechanical signaling. It is interesting that *Tbx1* regulates apical
368 constriction in the anterior DPW (Francou et al., 2017). Here, we show that *Fn1* regulates
369 the apical enrichment of actomyosin fibrils. Apical constriction is a known regulator of the
370 epithelial morphogenesis (Sawyer et al., 2010). Removal of the OFT leads to the
371 relaxation of cellular tension in the DPW (Francou et al., 2017); thus, we speculate that
372 the apical constriction at the anterior DPW is important for the generation of tissue tension
373 and, possibly, for the transitioning of DPW cells through the bent region connecting the
374 anterior DPW and the OFT.
375
376 The ablation of mesodermal Fn1 led to cell rounding, decreased cell volume,
377 downregulation of N-cadherin, and disrupted apical enrichment of actomyosin cables,
378 which altogether indicate diminished mechanical tension in the anterior DPW (Perez
379 Gonzalez et al., 2018). Nuclear accumulation of YAP was also disrupted in the mutants.
380 Cell adhesion to Fn1 regulates the activity of the Hippo pathway and promotes nuclear
381 localization of YAP (Kim and Gumbiner, 2015). However, the nuclear localization of YAP
382 is also affected by cell shape, and nuclear YAP is diminished upon cell rounding (Dupont,

383 2016). In Fn1$^{flox/-}$; *Mesp1*$^{Cre/+}$embryos, defects in cell shape and orientation are already
384 noted at E8.5 before the nuclear accumulation of YAP is detectable in these cells
385 (Francou et al., 2017). Therefore, our current experiments cannot discern whether
386 signaling by Fn1 signaling in the DPW regulates YAP nuclear translocation directly or
387 indirectly through the regulation of cell shape.
388
389 In *Xenopus Laevis* embryos, disruption of cadherin-mediated adhesions interferes with
390 Fn1 fibrillogenesis, resulting in tissue thickening and the shortening of the anterior-
391 posterior axis due to defects in cell shape, intercellular intercalations, and convergent
392 extension (Dzamba et al., 2009; Hirsh et al., 2018; Weber et al., 2011). Conversely,
393 disruption of Fn1 fibrillogenesis in fish and frog embryos leads to defective planar cell
394 polarity, cell shape, cadherin-mediated adhesion, and cell intercalation (Garavito-Aguilar
395 et al., 2010; Marsden and DeSimone, 2001; Marsden and DeSimone, 2003; Rozario et
396 al., 2009; Trinh and Stainier, 2004; Trinh et al., 2005). Our data are consistent with these
397 findings, indicating an evolutionary-conserved role of Fn1 and the crosstalk between cell-
398 cell and cell-ECM adhesions during tissue morphogenesis and cardiac development.
399
400 Although Fn1 synthesis is abolished in the mesoderm of Fn1$^{flox/-}$; *Mesp1*$^{Cre/+}$ embryos, the
401 levels of Fn1 protein at the basal side of the DPW recovered by E9.5, likely due to the
402 continued synthesis of *Fn1* mRNA by the adjacent endoderm. However, despite similar
403 levels of Fn1 protein underlying the DPW and the ~2-fold enrichment of Fn1 protein in the
404 anterior DPW of Fn1$^{flox/-}$; *Mesp1*$^{Cre/+}$ mutant embryos, Fn1 synthesized by the endoderm

405 (and by any other tissues) did not rescue defects in N-cadherin localization and cellular
406 architecture of the anterior DPW in these mutants, causing their demise by E10.75.
407 These results suggest that Fn1 synthesized by the mesoderm regulates epithelial
408 properties of the anterior DPW in a cell-autonomous manner. Altogether, our studies
409 support the notion that during morphogenesis, Fn1 regulates cell behaviors locally, in a
410 cell-autonomous manner, e.g., (Cseh et al., 2010; Turner et al., 2017; Wang and Astrof,
411 2016), and that Fn1 expressed by the anterior mesoderm is a central player coordinating
412 multiple cellular behaviors regulating the development of the DPW and the elongation of
413 the cardiac OFT.

Materials and Methods

Antibodies:

See Supplemental Table 1 for antibody information.

Ethics Statement

All experiments involving vertebrate animals were approved by the Rutgers University Institutional Animal Care and Use Committee and were performed following federal guidelines for the humane care of animals.

Mouse strains:

C57BL/6J mice (cat # 0664) and Rosa$^{mTmG/mTmG}$ mice, Gt(ROSA)26Sor$^{tm4(ACTB-tdTomato,-EGFP)Luo}$ mice (Cat# 037456) (Muzumdar et al., 2007), were purchased from Jackson Laboratories. Fn1$^{flox/flox}$ mice were a gift from Reinhardt Fassler (Sakai et al., 2001). Mesp1$^{Cre/+}$ knock-in mice (Saga et al., 1996; Saga et al., 1999) were obtained from Dr. Yumiko Saga. Fn1$^{+/-}$ strain (George et al., 1997; George et al., 1993) was a gift from Richard Hynes. Sox17$^{2A-iCre}$ mice were a gift from Heicko Lickert (Engert et al., 2009). For experiments, Fn1$^{+/-}$ mice were crossed with Mesp1$^{Cre/+}$ knock-in mice to generate Fn1$^{+/-}$; Mesp1$^{Cre/+}$ males which were propagated by mating with C57BL/6J females. To obtain embryos, Fn1$^{+/-}$; Mesp1$^{Cre/+}$ males were crossed with Fn1$^{flox/flox}$; Rosa$^{mTmG/mTmG}$ females, and pregnant females were dissected at days specified in the figures. Mice and embryos were genotyped according to published protocols (Engert et al., 2009; George et al., 1993; Saga et al., 1999). Embryos were staged by counting somites.

437

438

439 *Cell culture and generation of cell lines:*

440 Mouse embryo fibroblasts (MEFs) were isolated from E13.5 embryos resulting from the
441 mating of $Fn1^{+/-}$ mice with $Fn1^{flox/flox}$; $ROSA^{mTmG/mTmG}$ mice.

442 MEFs were cultured on plates pre-coated with 0.1% gelatin (Sigma, #G1890) dissolved
443 in H_2O and maintained in complete medium, which consisted of Dulbecco's Modified
444 Eagle's medium (DMEM) with 4.5 g/L glucose, L-glutamine & sodium pyruvate (Corning,
445 #10-013-CM) supplemented with 100 U/ml penicillin, 100 μg/ml streptomycin (Gibco,
446 #15140-122), 1% v/v GlutaMax (L-glutamin, Gibco, #35050061) and 10% v/v fetal bovine
447 serum (FBS, Gemini Biosciences, #100-106) in a humidified incubator with 5% CO_2 at
448 37°C.

449

450 To generate MEFs lacking Fn1 (Fn1-null), or control, Fn1-heterozygous (Fn1-het) MEFs,
451 $Fn1^{flox/+}$; $ROSA^{mTmG/+}$ and $Fn1^{flox/-}$; $ROSA^{mTmG/+}$ MEFs were infected with
452 adenoviruses encoding Cre recombinase, Ad-Cre-IRED-GFP (Vector Biolabs, #1710).
453 Cre-induced recombination not only leads to the ablation of Fn1 by recombining the floxed
454 Fn1 sequence but also induces the expression of membrane-tethered GFP in these cells.
455 For this experiment, $3x10^4$ MEFs were plated on gelatin-coated wells of 6-well plates. 24
456 hours later, cells were rinsed twice with Phosphate Buffered Saline 1X Sterile Solution
457 (PBS, RPI Research Products, # P10400-500) and infected with Cre adenovirus diluted
458 to the multiplicity of infection of 500 in DMEM without FBS. 20 hours post-infection, the
459 medium was replaced by the complete medium. Although each of these cell types carries

460 one ROSA^{mTmG} allele, only cells infected with Ad-Cre are constitutively and permanently
461 marked by the expression of GFP due to the recombination of the reporter locus. GFP
462 expression from the adenovirus is transient and dissipates after three days post-infection.
463 After expansion, Ad-Cre-treated cells were sorted to generate Fn1$^{\Delta/-}$ (Fn1-null, GFP+),
464 Fn1$^{flox/-}$ (Fn1-heterozygous, GFP-), Fn1 $^{\Delta/+}$ (Fn1-heterozygous, GFP+), and Fn1$^{flox/+}$ (Fn1-
465 wild type, GFP-) MEF lines. Western blot analysis was used to assay Fn1 expression.
466
467 *MEF protein lysates:*
468 Cells were plated in 6-well dishes at a density of 2×10^5 cells per well. After 48 hours, cells
469 were washed twice with cold PBS supplemented with 0.1 mM $CaCl_2$ and 1 mM
470 $MgCl_2$ (PBS-Ca^{2+}/Mg^{2+}) and lysed with 400 μl of RIPA lysis buffer (50 mM Tris-Cl, 150
471 mM NaCl, 2 mM EDTA, 1% v/v NP-40, 0.5% w/v sodium deoxycholate, 0.1% w/v SDS,
472 1X protease inhibitor cocktail (Cell Signaling Technology, #5871), pH 8.0).
473 The samples were centrifuged at 16,000 × g for 15 min at 4°C.
474 Protein concentration was determined using BCA protein assay (Pierce™ BCA Protein
475 Assay Kit, #23225). Then, lysis buffer was added to equalize protein concentration across
476 samples. 4xNuPAGE™ LDS Sample buffer (Thermo Scientific, #NP0008) with 10% β-
477 mercaptoethanol (Sigma, #63689) was added to each sample to the final concentration
478 of 1X NuPAGE and 2.5% β-mercaptoethanol. Samples were heated to 95°C for 5 minutes
479 prior to loading on gels.
480
481 *Immunoblotting and densitometry quantification:*

482 For immunoblotting, samples were resolved using 4-12% Tris-Glycine gel (Invitrogen,
483 #XP04120BOX) at 130 V in 1x Tris-Glycine SDS Running Buffer (Invitrogen, # LC2675)
484 for 1 hour 30 minutes. Proteins were then transferred to nitrocellulose membranes with a
485 0.2 µm pore size (Bio-Rad, # 1620122) and 1x Tris-Glycine, 15% methanol transfers
486 buffer (10x Tris-Glycine buffer: 30g Tris Base. 144 g Glycine in 1L of ddH20, pH: 8.5).
487 The transfer was carried out at 90 V for 2 hours in ice.
488 After the transfer, the nitrocellulose membranes were blocked with Intercept Blocking
489 Buffer (Li-Cor, # 927-60001) for 1 hour. Primary antibodies were diluted in Intercept
490 Antibody Diluent (Li-Cor, # 927-65001) and incubated overnight at 4°C. After 24h, the
491 nitrocellulose membranes were washed three times with PBS containing 0.1% Tween for
492 10 min. We used IRDye 680RD Donkey anti-Rabbit IgG (#926-68073), and IRDye
493 800CW Donkey anti-Mouse IgG Secondary Antibody (#926-32212) as secondary
494 antibodies in a 1:15000 dilution in Intercept Antibody Diluent (Li-Cor, # 927-65001). The
495 nitrocellulose membranes were incubated with the secondary antibodies for 1 hour at
496 room temperature. Finally, membranes were washed three times with PBS 0.1% Tween
497 for 10 minutes and imaged using Li-Cor Odyssey 9120 Gel Imaging System (#ODY-
498 2425). The density of unsaturated pixels was determined using ImageJ software (version
499 2.1.0/1.53c4). For each condition, protein bands were quantified from at least three
500 independent experiments.
501
502 *Cell surface biotinylation:*
503 $3.5x10^5$ cells were plated on gelatin-coated 10 cm plates. After 48 hours of growth, cells
504 were washed twice with ice-cold PBS supplemented with 0.1 mM $CaCl_2$ and 1 mM $MgCl_2$

505 (PBS-Ca^{2+}/Mg^{2+}), followed by incubation with 1 mM EZ-Link Sulfo-NHS-LC-Biotin
506 (Thermo Scientific, #21335) in PBS-Ca^{2+}/Mg^{2+} for 30 min at 4°C. The biotinylation
507 reaction was quenched by incubating cells with Tris-buffered solution (50 mM Tris-HCl,
508 pH 7.4) for 10 min at 4°C. After two subsequent washes with PBS-Ca^{2+}/Mg^{2+}, cells were
509 lysed with 600 μl of RIPA lysis buffer (50 mM Tris-Cl, 150 mM NaCl, 2 mM EDTA, 1% v/v
510 NP-40, 0.5% w/v sodium deoxycholate, 0.1% w/v SDS, 1X protease inhibitor cocktail (Cell
511 Signaling Technology, #5871), pH 8.0). To remove insoluble material, cell extracts were
512 clarified by centrifugation at 16,000 x g for 15 min at 4°C. Soluble biotinylated protein
513 concentration was determined using BCA protein assay (Pierce™ BCA Protein Assay Kit,
514 #23225). 300 µg of protein per sample was incubated with 40 µl of Neutravidin-Agarose
515 beads (Thermo Scientific, # 29202) pre-washed with RIPA lysis buffer. After 1 hour of
516 incubation at 4°C, the Neutravidin-Agarose beads were washed 3 times with RIPA lysis
517 buffer containing 1X protease inhibitor cocktail. 120 µl of 1X NuPAGE™ LDS Sample
518 buffer (Thermo Scientific, #NP0008) with 2.5% β-mercaptoethanol (Sigma, #63689) and
519 1X protease inhibitor cocktail was added to beads and resolved by SDS-PAGE (Arriagada
520 et al., 2020).
521
522 *Immunofluorescence microscopy:*
523 $2x10^4$ cells were plated on gelatin-coated #1.5 round glass coverslips (Fisher Scientific,
524 t#12-545-81) in 24-well dishes. After for 48 hours, cells were washed with PBS that was
525 pre-warmed to 37°C for 5 minutes and fixed with 4% PFA (Fisher Scientific # 50-980-487,
526 diluted in PBS) for 20 minutes at room temperature. Then, cells were washed three times
527 with PBS for 5 minutes each and permeabilized with PBS containing 0.1% Triton-X 100

528 (PBST) for 15 minutes. Cells were blocked with 5% Donkey serum (Sigma, #d9663) in
529 PBST (blocking solution) for 30 minutes. After blocking, cells were incubated with the
530 primary antibodies diluted in blocking solution overnight at 4°C. Following 3 washes in
531 PBST for 10 minutes each, cells were incubated with secondary antibodies diluted in
532 blocking solution for 60 minutes at room temperature. Finally, cells were washed three
533 times with PBST for 10 minutes, mounted using a 50% v/v Glycerol, 50% v/v Methanol
534 solution.
535
536 *Wound healing migration assay:*
537 $1x10^4$ cells were plated on gelatin-coated 8-well ibidi dishes (Ibidi, #80827) for 72 hours.
538 When cells were confluent, the monolayer was scratched with a sterile 10 µl pipette tip.
539 Cell debris was washed out with PBS, and incubated with imaging medium 100 µl
540 FluoroBrite DMEM (Thermo Fisher Scientific, #A1896701) supplemented with 100 U/ml
541 penicillin, 100 µg/ml streptomycin (Gibco, #15140-122), 1% v/v GlutaMax (L-glutamin,
542 Gibco, #35050061) and 2% v/v fetal bovine serum (FBS, Gemini Biosciences, #100-106).
543 Images were acquired right after performing the scratch and then after 14 hours. % of
544 wound closure was measured. % of Wound closure = $100*(A_{t=0} - A_{t=14})/ A_{t=0})$
545 *Where $A_{t=0}$ is the cell-free area at t=0 and $A_{t=14}$ is the cell-free area at t=14 hrs.*
546
547 *Whole Mount Immunofluorescence staining:*
548 Timed matings were set up to obtain embryos at specific embryonic stages. Vaginal plugs
549 were checked daily, and noon of the day the plug was found was an embryonic day (E)
550 0.5 of gestation. Embryo dissections were aided using a Zeiss Stemi 2000C

551 stereomicroscope. Embryos were dissected into ice-cold PBS; yolk sacs were kept for
552 genotyping. After dissection, embryos were fixed with 4% PFA overnight at 4°C. Then,
553 embryos were washed two times with ice-cold PBS and permeabilized with PBS
554 containing 0.1% Triton- X 100 (PBST) overnight at 4°C. Embryos were blocked with 10%
555 Donkey serum in PBST (blocking solution) overnight at 4°C. After blocking, embryos were
556 incubated with the primary antibodies diluted in blocking solution for 3 days at 4°C.
557 Following four 1 hour-washes with PBST, embryos were incubated with secondary
558 antibodies diluted in blocking solution for 3 days at 4°C. Finally, after four washes with
559 PBST for 1 hour each, embryos were embedded in 1% agarose (Bio-Rad Laboratories,
560 #1613101), and cleared using methanol and Benzyl Alcohol (Sigma, # B-1042)/ Benzyl
561 Benzoate (Sigma, #B-6630) as described (Ramirez and Astrof, 2020). For imaging,
562 embryos were a placed between two #1.5 coverslips (VWR, #16004-312) separated by a
563 rubber spacer (Grace Bio Labs, # 664113).
564
565 *Whole Mount Immunofluorescence in situ hybridization:* After dissection, embryos were
566 fixed with 4% PFA overnight at 4°C and washed twice with PBS. *In situ hybridization*
567 assay carried out using the RNAscope® Multiplex Fluorescent v2 reagents (Advanced
568 Cell Diagnostics, # 323110) as previously described (Nomaru et al., 2021). We used a
569 C1 probe for Fn1 (#408181).
570
571 *Embryo Cryosection and immunofluorescence staining:*
572 After dissection, embryos were fixed with 4% PFA overnight at 4°C and washed twice
573 with PBS. Embryos were then incubated with 10% sucrose in PBS for 4 hours at room

574 temperature and then with 20% sucrose in PBS overnight at 4°C with agitation. Embryos
575 were then incubated with 30% sucrose in PBS for 4 hours at room temperature, and then
576 with a 1:1 mixture of Tissue-Tek O.C.T. Compound (O.C.T, Sakura, #4583) and 30%
577 sucrose solution for 1 hour at room temperature with agitation. Finally, embryos were
578 placed into 100% O.C.T for 10-20 minutes without agitation. Embryos were then
579 positioned in fresh 100% OCT solution in plastic molds and frozen by dipping the mold
580 into 2-methyl butane chilled on dry ice. 8 µm-thick sections were obtained using a Leica
581 CM1950 Cryostat. For long term storage, slides were kept at -80°C. For
582 immunofluorescence, we used an ImmEdge Hydrophobic Pen (VWR, 101098-065) to
583 draw a hydrophobic barrier around tissue sections. Tissue sections were permeabilized
584 by washing with PBS containing 0.05% Tween-20 (Sigma, cat # P7949) 3 times for 5
585 minutes. Then, slides were placed in a humidified chamber, and sections were incubated
586 with a blocking buffer containing 5% donkey serum in PBS-0.05% Tween for 30 minutes
587 at room temperature. The blocking buffer was then removed and replaced with primary
588 antibodies diluted in blocking buffer and incubated with sections overnight at 4°C. After
589 washing the slides 3 times for 5 minutes with PBS-0.05% Tween; sections were incubated
590 with secondary antibodies for 1 hour at room temperature. Finally, slices were washed 3
591 times for 5 minutes each with PBS-0.05%Tween and mounted using a 50% v/v Glycerol,
592 50% v/v Methanol solution. Sections stained with SiR-Actin (Cytoskeleton, #CY-SC001,
593 2µM), samples were mounted with Vectashield Antifade Mounting Medium (Vector
594 laboratories, #H-1000).
595
596 *TUNEL assay:*

597 TUNEL assay was performed using the In Situ Cell Death Detection Kit from Roche (cat
598 #11684795910) following manufacturer's instructions.
599
600 *Imaging, quantifications, and statistical analyses:*
601 Embryos were imaged using confocal microscopy using Nikon A1R microscope with 20x
602 CFI Apo LWD Lambda S water immersion objective (#MRD77200) or 25x CFI Plan Apo
603 Lambda S silicone oil objectives (#MRD73250). Cultured cells were imaged using
604 confocal microscopy and the Plan Fluor 567 40x Oil immersion objective (numerical
605 aperture 1.3, # MRH01401). 3D reconstructions, surfacing, and quantifications were
606 performed using IMARIS software (Bitplane, USA). Fluorescence intensity and angles
607 were measured using Fiji software and plotted using Orient software, version 3.1.1. Cell
608 ellipticity was measured using Imaris as described (Andrews et al., 2021). Statistical
609 analyses were performed using Prism 9, version 9.4.1 (GraphPad Software, LLC).
610
611 *Embryo protein extract:*
612 Embryos were lysed with 100 µL of SDS lysis buffer (0.1 M Tris-HCl, 0.2% SDS, 5mM
613 EDTA pH 8 containing 1X protease inhibitor cocktail and homogenized by drawing the
614 lysates 10 times though a 27G syringe. 33.3 µl of 4X NuPAGE™ LDS Sample buffer
615 containing 10% β-mercaptoethanol were added to each sample, samples were incubated
616 at 95°C for 5 minutes.
617

Acknowledgments: We thank Sam Russo for help with mouse colony maintenance and genotyping. We thank members of the Astrof lab for their careful reading of the manuscript and for helpful comments and suggestions throughout this work.

Figures Legends

Figure 1. The expression of Fn1 in Mesp1 lineage is required for the OFT elongation.

$Fn1^{flox/+}$; $Mesp1^{Cre/+}$ (Control) and $Fn1^{flox/-}$; $Mesp1^{Cre/+}$ (Mutant) embryos were dissected at E9.5 and staged according to somite number. **A-D.** Embryos between 18-19 somites. n=5 controls and 4 mutants. **E-H.** Embryos between 20-25 somites, n= 5 control and 7 mutant embryos. Imaris was used to surface distal OFT (yellow), proximal OFT (turquoise), and the left ventricle and atria (pink)**. C-D, G-H.** The length of the distal and proximal OFT in each embryo was normalized to the height of the left ventricle to control for embryo size. **I-J.** $Fn1^{flox/+}$; $Mesp1^{Cre/+}$ (Control) and $Fn1^{flox/-}$; $Mesp1^{Cre/+}$ (Mutant) embryos were dissected at E9.5 (20-25s) and stained with DAPI and the MF-20 antibody. **K**. Quantification of angles in controls and mutants as shown in **I-J**. n= 9 controls and 13 mutants. Means (horizontal bars) and standard deviations (error bars) are displayed; p was calculated using a 2-tailed, unpaired Student's t-test. OFT-outflow tract, MF-20 antibody detects sarcomeric myosin heavy chain. All scale bars : 200 mm

640 **Figure 2. The expression of Fn1 in the mesoderm is important for the regulation of**
641 **cell shape in the anterior DPW at E8.5**. **A.** $Fn1^{flox/+}$; $Mesp1^{Cre/+}$ (Control) and **E.** $Fn1^{flox/-}$
642 ; $Mesp1^{Cre/+}$ (Mutant) embryos were dissected at E8.5 (9-11s) and stained to detect GFP
643 (green) and nuclei (DAPI, blue). Regions marked by dashed rectangles in **A, B** are
644 magnified in **A1-E1** and **A2-E2**. **B-C, F-G.** Outlines of aDPW and pDPW cells. **D** and **H**.
645 3D reconstruction of aDPW cells. **I-L.** Cell shape. Small dots mark data points from each
646 cell; large dots mark the average per embryo. Data points from one embryo are marked
647 with the same color. **I-J**. Cell circularity. **I.** 320 cells from 5 control and 367 cells from 5
648 mutant embryos were analyzed. **J.** 311 cells from 5 control and 326 cells from 5 mutant
649 embryos were analyzed. **K-L.** Ellipticity and volume of aDPW cells; 51 cells from 5 control
650 and 50 cells from mutant embryos were analyzed. Means (horizontal bars) and standard
651 deviations (error bars) are displayed; p was calculated using a 2-tailed, unpaired
652 Student's t-test. OFT-outflow tract, aDPW-anterior dorsal pericardial wall, pDPW-
653 posterior dorsal pericardial wall, A-atrium, V-ventricle.
654
655 **Figure 3. Expression of Fn1 in the mesoderm regulates Golgi apparatus orientation**
656 **in the anterior DPW. A-A2.** $Fn1^{flox/+}$; $Mesp1^{Cre/+}$ (Control) and **B-B2**. $Fn1^{flox/-}$; $Mesp1^{Cre/+}$
657 (Mutant) embryos were dissected at E8.5 (9-11s) and stained to detect GFP (green),
658 GM130 (white), and nuclei (DAPI, blue). Boxes in **A, B** are magnified in the panels **A1-**
659 **A2,** and **B1-B2.** Arrows point to Golgi. **A3, A4, B3, B4**. Semicircular histograms represent
660 the distribution of the Golgi orientation angles in DPW cells that were measured as
661 indicated in **C**. N=total number of cells analyzed in 3 controls and 3 mutants. **D, E**.
662 Quantification of Golgi polarization. Golgi was considered polarized if the angle between

663 the Golgi and the plane of the endoderm fell between 85^0 and 95^0. OFT-outflow tract,
664 aDPW-anterior dorsal pericardial wall, pDPW-posterior dorsal pericardial wall, A-atrium,
665 V-ventricle
666
667 **Figure 4. Expression of Fn1 in the mesoderm regulates cell polarity in the anterior**
668 **DPW. A.** $Fn1^{flox/+}$; $Mesp1^{Cre/+}$ (Control) and **B.** $Fn1^{flox/-}$; $Mesp1^{Cre/+}$ (Mutant) embryos were
669 dissected at E8.5 (9-11s), and stained to detect GFP (green), podocalyxin (white), and
670 nuclei (DAPI, blue). Boxes in **A** and **B** were expanded in **A1** and **B1** to show the anterior
671 DPW and in **A2** and **B2** to show the posterior DPW. Arrows in **A1** point to cells with apical
672 localization of podocalyxin. Arrows in **B1** point to defective basolateral localization of
673 podocalyxin in mutants. **A2, B2.** Podocalyxin is localized apically in the posterior DPW,
674 arrows. **C-D** Quantification of cells with defective podocalyxin localization in the anterior
675 and posterior DPW. **C.** 148 cells in the aDPW from 3 controls and 224 cells in aDPW from
676 3 mutants were analyzed. **D.** 149 cells in the pDPW from 3 controls and 182 cells in the
677 pDPW from 3 mutants were analyzed. Each small dot represents data from one slice, and
678 each large dot is an average of all slices per embryo. Data from the same embryo is
679 marked by the same color. **E-G.** $Fn1^{flox/+}$; $Mesp1^{Cre/+}$ (Control) and **H-J.** $Fn1^{flox/-}$; $Mesp1^{Cre/+}$
680 (Mutant) embryos were dissected at E8.5 (7-8s), and stained for GFP (green), aPKC,
681 laminin g1, and nuclei (DAPI, blue). Arrows in **F** point to apical localization of aPKC in
682 control DPW cells. **I.** Arrows point to defective basolateral localization of aPKC in mutants.
683 Arrowheads in **G** point to basal localization of laminin g1 in controls and in **J** to
684 disorganized localization of laminin g1 in one of three mutants. **K.** Quantification of cells
685 in which aPKC was re-distributed away from the apical surface. DPW cells from 5 different

686 slices were evaluated in 3 control and 3 mutant embryos. Each small dot represents data
687 from one slice, and each large dot is an average of all slices per embryo. Data from the
688 same embryo is marked by the same color. Means (horizontal bars) and standard
689 deviations (error bars) are displayed; p was calculated using a 2-tailed, unpaired
690 Student's t-test. OFT-outflow tract, aDPW-anterior dorsal pericardial wall, pDPW-
691 posterior dorsal pericardial wall, A-atrium, V-ventricle.
692
693 **Figure 5. Mesodermal Fn1 regulates the expression of N-Cadherin at cell-cell**
694 **junctions in the DPW. A-B.** $Fn1^{flox/+}$; $Mesp1^{Cre/+}$ (Control) and **C-D.** $Fn1^{flox/-}$; $Mesp1^{Cre/+}$
695 (Mutant) embryos were dissected at E9.5 (21-26s) and stained to detect GFP (green), N-
696 cadherin (white) and nuclei (DAPI, blue). Junctional N-Cadherin is enriched in the anterior
697 DPW (boxed region in **B**). Boxes in **B**-**D** are expanded in **B1** and **D1.** Arrows point to
698 DPW. **E.** Western blot analysis of total cell lysates and cell surface proteins. Positions of
699 molecular weight markers are indicated on the left. **F-G**. Densitometrical quantification of
700 immunoblot signals. N = 4 for each genotype. Each experiment is represented by a dot
701 of a different color. Means (horizontal bars) and standard deviations (error bars) are
702 displayed; 2-tailed, unpaired Student's t-tests were used to determine p values. **H-K.**
703 Immunostaining to detect GFP (green), N-cadherin (white), and nuclei (DAPI, blue) in
704 $Fn1^{flox/-}$, $Fn1^{\Delta/-}$ (Fn1-null), $Fn1^{flox/+}$ and $Fn1^{\Delta/+}$ MEFs. Boxes in **I-K** and in **M-O** are
705 expanded in **I1-K1 and M1-O1.** Arrows point to N-cadherin at cell borders in control MEFs
706 (**I1, M1, and O1**) and to the absence of N-cadherin at cell borders in $Fn1^{\Delta/-}$ MEFs (**K1**).
707 DPW- dorsal pericardial wall, OFT-outflow tract, A-atrium.
708

709 **Figure 6. Mesodermal Fn1 regulates the length and organization of F-actin in the**
710 **anterior DPW. A-B1.** $Fn1^{flox/+}$; $Mesp1^{Cre/+}$ (Control) and **C-D1.** $Fn1^{flox/-}$; $Mesp1^{Cre/+}$
711 (Mutant) embryos were dissected at E9.5 (21-26s), and transverse cryosections (a plain
712 of sections shown by the dashed line in **E**) from the anterior DPW were stained to detect
713 GFP (green), F-actin (white), and nuclei (DAPI, blue). Yellow arrows point to F-actin in
714 the DPW in **B1** and **D1**. Yellow arrowheads point to apically enriched F-actin in **B1** and
715 re-distributed F-actin in **D1**. **E.** Schematic representation of different regions in the DPW.
716 **F-H.** Traces of F-actin in control and mutants. **G-I.** Angles made by F-actin filaments
717 relative to cells' apical surface were measured. **J.** Quantification of actin polarization. An
718 F-actin filament was considered polarized if it was between 85 and 95 degrees relative to
719 the apical surface of the DPW. **K** Quantification of the F-actin length in the anterior DPW;
720 235 cells from 3 controls and 417 cells from 5 mutants were examined. Small dots mark
721 the F-actin length of individual cells, and large dots mark the average per slice. Dots from
722 the same embryo are displayed in the same color. Means (horizontal bars) and standard
723 deviations (error bars) are displayed; p was calculated using a 2-tailed, unpaired
724 Student's t-test. DPW-dorsal pericardial wall, A-atrium, NT-Neural tube, AVC-
725 atrioventricular canal, OFT-outflow tract, V-ventricle.
726
727 **Figure 7 Mesodermal Fn1 regulates the expression of pMLC in the anterior DPW.**
728 **A-B2.** $Fn1^{flox/+}$; $Mesp1^{Cre/+}$ (Control) and C-D. $Fn1^{flox/-}$; $Mesp1^{Cre/+}$ (Mutant) embryos were
729 dissected at E9.5 (21-26s), and sagittal cryosections were stained to detect GFP (green),
730 F-actin (white) and nuclei (DAPI, blue). Boxes in **A-B** were expanded in **B1** and **B2** to
731 show the anterior and posterior DPW, respectively. Boxes in **C-D** were expanded, in **D1**

732 and **D2**, to show the anterior and posterior DPW, respectively. Arrows point to the apical
733 enrichment of F-actin in the anterior and posterior of controls and the lack of such
734 enrichment in the anterior DPW of the mutants (**D1**). 6 controls and 3 mutants were
735 analyzed. **E-H2**. $Fn1^{flox/+}$; $Mesp1^{Cre/+}$ (Control) and **C-D.** $Fn1^{flox/-}$; $Mesp1^{Cre/+}$ (Mutant)
736 embryos were dissected at E9.5 (21-26s) and sagittal cryosections were stained to detect
737 GFP (green), pMLC (white) and nuclei (DAPI, blue). Boxes in **E-F** are expanded in **F1**
738 and **F2** to show the anterior and posterior DPW, respectively. Boxes in **G-H** are expanded
739 in **H1** and **H2** to show anterior and posterior DPW, respectively. Arrows in **F1** indicate
740 cells with apical localization of pMLC. Arrows in **H1** show a defective basolateral
741 localization of pMLC in mutants. **F2, H2**. pMLC is localized apically in the posterior DPW.
742 8 controls and 3 mutants were analyzed.
743
744 **Figure 8. Mesodermal Fn1 regulates nuclear localization of YAP. A. Ventral view of**
745 **E9.5 embryo.** YAP localization was assayed in the DPW between the left and the right
746 limits (marked by the vertical lines).
747 **B-B2.** $Fn1^{flox/+}$; $Mesp1^{Cre/+}$ (Control) and **C-C2.** $Fn1^{flox/-}$; $Mesp1^{Cre/+}$ (Mutant) embryos were
748 dissected at E9.5 (23-26s) and stained to detect nuclei (DAPI, magenta) and YAP (cyan).
749 Regions outlined by dashed rectangles are expanded in **B1, C1** (anterior DPW) and **B2,**
750 **C2** (posterior DPW). **D-E**. Quantification of the intensity ratio between nuclear and
751 cytosolic YAP in the aDPW and pDPW. 7-8 optical slices from 4 controls and 7-8 optical
752 slices from 4 mutant embryos were analyzed. Each small dot represents one slice, and
753 each large dot is an average of all slices in one embryo. Data from the same embryo is
754 marked by the same color. **F.** Summary: YAP is enriched in the nuclei in the presence of

755 both the mesodermal (red lines) and endodermal (blue lines) Fn1. In the absence of
756 mesodermal Fn1, nuclear translocation of YAP are decreased. aDPW- anterior dorsal
757 pericardial wall, pDPW-posterior dorsal pericardial wall, OFT-outflow tract.
758
759 **Figure 9. Mesodermal Fn1 is required for DPW cell proliferation. A-C.** $Fn1^{flox/+}$;
760 $Mesp1^{Cre/+}$ (Control) and **D-F** $Fn1^{flox/-}$; $Mesp1^{Cre/+}$ (Mutant) embryos were dissected at E9.5
761 (20-25s) and stained for PHH3 (white), and nuclei (DAPI, blue) E9.5 (20-25s). **A,B, D, E**.
762 DPW (magenta) and $PHH3^{+}$ cells in the DPW (white) were segmented using Imaris. **C,F**.
763 Proportion of PHH3+ cells in the aDPW (magenta) and pDPW (turquoise) were quantified
764 in **G-H**. Each dot marks one embryos. n=4 control and 6 mutant embryos. Means
765 (horizontal bars) and standard deviations (error bars) are displayed, 2-tailed, unpaired
766 Student's t test was used to determine p values. aDPW-anterior dorsal pericardial wall,
767 pDPW- posterior dorsal pericardial wall, PHH3- Phosphorylated Histone H3.
768
769 **Figure 10. Expression patterns of *Fn1 mRNA* and protein in controls and mutants**.
770 **A-J.** Expression of *Fn1 mRNA*. Embryos were dissected at E9.5 (23-26s) and labeled
771 with DAPI (magenta) and anti-sense Fn1 probe (turquoise). **A-B2** $Fn1^{flox/+}$; $Mesp1^{+/+}$
772 (designated as WT), **C.** *Fn1 mRNA* intensity ratio between aDPW and pDPW, **D-F2.**
773 $Fn1^{flox/+}$; $Mesp1^{Cre/+}$ (Control) **G.** *Fn1 mRNA* intensity in the anterior (**H**) and posterior (**J**)
774 DPW was normalized to that in the endoderm. 6 different slices from 3 WT, 4 control and
775 9 mutant embryos were analyzed. **H-I2.** $Fn1^{flox/-}$; $Mesp1^{Cre/+}$ (Mutant) embryos. Regions
776 outlined by the dotted rectangles in **B, E,** and **I** are expanded in panels to the right and
777 color-coded according to fluorescence intensity (scale is on the right). White arrows point

778 to DPW. Yellow arrowheads point to the endoderm. **K.** Ventral view of the DPW, Fn1
779 expression is color-coded according to fluorescence intensity. **L.** Ratio of Fn1 protein
780 intensity shows similar enrichment of Fn1 in the anterior DPW of controls and mutants.
781 **M, M1.** $Fn1^{flox/+}$; $Mesp1^{Cre/+}$ (Control) and **N, N1.** $Fn1^{flox/-}$; $Mesp1^{Cre/+}$ (Mutant) embryos
782 were dissected at E9.5 (22-26s) and stained to detect Fn1 protein (white) and nuclei
783 (DAPI, blue). Fn1 protein expression in the DPW (**M, N**) is color-coded according to
784 fluorescence intensity in **M1, N1**. **O-P.** Fn1 protein levels underlying the anterior DPW are
785 unchanged in the mutants. Fn1 intensity in the aDPW and pDWP regions outlined by the
786 red dash lines in **M1-N1** was normalized by DAPI intensity; 7 optical slices from 8 control
787 and 10 mutant embryos were evaluated. Each small dot represents one slice, and each
788 large dot is an average of all slices per embryo. Data from the same embryo is marked
789 by the same color. Means (horizontal bars) and standard deviations (error bars) are
790 displayed, 2-tailed, unpaired Student's t-test was used to determine p values. aDPW-
791 anterior dorsal pericardial wall, pDPW- posterior dorsal pericardial wall, OFT-outflow tract,
792 A-atrium, LV-left ventricle.
793
794 **Figure 11. The central role of the mesodermal Fn1 in regulating the elongation of**
795 **the cardiac outflow tract.** Fn1 synthesized by the mesoderm mediates the elongation
796 of the cardiac outflow tract by regulating cell shape, polarity, proliferation, and
797 mechanotransduction in the anterior dorsal pericardial wall (aDPW).
798
799 **Figure S1. $Fn1^{flox/-}$; $Mesp1^{Cre/+}$ mutant embryos do not survive past E10.75 of**
800 **gestation.**

801 **A.** Schematic representation of a sagittal section. **B-B1** Fn1$^{flox/+}$; Mesp1$^{Cre/+}$ (Control) and
802 **C-D1** Fn1$^{flox/-}$; Mesp1$^{Cre/+}$ (Mutant) embryos dissected at E9.5. **E-E1.** Fn1$^{flox/+}$; Mesp1$^{Cre/+}$
803 (Control) and **F-F1** Fn1$^{flox/-}$; Mesp1$^{Cre/+}$ (Mutant) embryos dissected at E10.75. **G.**
804 Genotype distributions of embryos isolated at different stages of gestation. dOFT-distal
805 outflow tract, pOFT- proximal outflow tract, aDPW-anterior dorsal pericardial wall, pDPW-
806 posterior dorsal pericardial wall, A-atrium.
807
808 **Figure S2. The initial formation of the cardiac outflow tract is not affected by the**
809 **deletion of Fn1 in the mesoderm at E8.5. A-B**. Illustration of our method for measuring
810 OFT dimensions. Fn1$^{flox/+}$; Mesp1$^{Cre/+}$ (Control) embryo at E9.5. Imaris was used to
811 surface the Distal OFT (yellow), Proximal OFT (turquoise) and the left ventricle and atria
812 (pink). White lines show how the length of OFT segments and LV were measured. **C-C1**
813 Fn1$^{flox/+}$; Mesp1$^{Cre/+}$ (Control) and **D-D1** Fn1$^{flox/-}$; Mesp1$^{Cre/+}$ (Mutant) embryos were
814 dissected at E8.5. Imaris was used to surface the OFT (yellow) and the left ventricle and
815 atria (pink). **E.** The length of the OFT was normalized to the height of the left ventricle to
816 control for embryo size. 11 control and 11 mutant embryos were analyzed. Each dot
817 corresponds to one embryo. Means (horizontal bars) and standard deviations (error bars)
818 are displayed p was calculated using 2-tailed, unpaired Student's t-test. OFT- outflow
819 tract.
820
821 **Figure S3. Mesodermal Fn1 regulates DPW cell shape at E9.5**. **A.** Fn1$^{flox/+}$; Mesp1$^{Cre/+}$
822 (Control) and **E.** Fn1$^{flox/-}$; Mesp1$^{Cre/+}$ (Mutant) embryos were dissected at E9.5 (21-25s)
823 and stained to detect GFP (green) and nuclei (DAPI, blue). Regions marked by dashed

824 rectangles in **A, B** are magnified in **A1-E1** and **A2-E2**. **B-C, F-G.** Outlines of aDPW and
825 pDPW cells. **D** and **H.** 3D reconstruction of aDPW cells. **I-L.** Cell shape analyses. Small
826 dots mark a data point from each cell; large dots mark the average per embryo. Data
827 points from one embryo are marked with the same color. **I-J**. Cell circularity. **I.** 396 cells
828 from 5 control and 436 cells from 5 mutant embryos were analyzed. **J.** 390 cells from 5
829 control and 419 cells from 5 mutant embryos were analyzed. **K-L.** Ellipticity and volume
830 of aDPW cells. n=10 cells from 5 control and 10 cells from 5 mutant embryos were
831 analyzed. Means (horizontal bars) and standard deviations (error bars) are displayed; p
832 was calculated using a 2-tailed, unpaired Student's t-test. OFT-outflow tract, aDPW-
833 anterior dorsal pericardial wall, pDPW-posterior dorsal pericardial wall, A-atrium.
834
835 **Figure S4. Mesodermal depletion of Fn1 does not alter the number of basal**
836 **protrusions in the aDPW. A.** $Fn1^{flox/+}$; $Mesp1^{Cre/+}$ (Control) and **B.** $Fn1^{flox/-}$; $Mesp1^{Cre/+}$
837 (Mutant) embryos were dissected at E9.5 (21-26s), and transverse cryosections from the
838 anterior DPW were stained to detect GFP (black). Red rectangles in **A, B** are expanded
839 in **A1** and **B1**. Arrows point to protrusion extending from the basal membranes of aDPW
840 cells. **C.** Quantification of the number of protrusions normalized for the length of the DPW.
841 n= 3 control and 4 mutant embryos. 2 – 7 sections per embryo were analyzed. Small dots
842 mark the number of protrusions in each section. Large dots mark the mean in each
843 embryo. Data from the same embryo is marked with the same color. P was calculated
844 using a 2-tailed, unpaired Student's t-test. aDPW- anterior dorsal pericardial wall. P was
845 calculated using a 2-tailed, unpaired Student's t-test.

846 **Figure S5. mesodermal Fn1 do not regulates cell polarity in the DPW at E9.5 . A.**
847 $Fn1^{flox/+}$; $Mesp1^{Cre/+}$ (Control) and **B.** $Fn1^{flox/-}$; $Mesp1^{Cre/+}$ (Mutant) embryos were dissected
848 at E9.5 (19-24s), and stained to detect GFP (green), podocalyxin (white), and nuclei
849 (DAPI, blue). Boxes in **B** and **D** were expanded in **B1** and **D1**. Arrows show apical
850 localization of podocalyxin in control and mutant embryos. **E** Quantification of cells with
851 defective podocalyxin localization in the anterior and posterior DPW. P was calculated
852 using a 2-tailed, unpaired Student's t-test; $p \geqslant 0.05$ indicates a non-significant difference
853 between the two groups. DPW- dorsal pericardial wall, A- atrium, NT- Neural tube, OFT-
854 outflow tract.
855
856 **Figure S6. Generation of MEF lines . A-B.** Schematic representation of resultant alleles
857 upon Cre recombination in $Fn1^{flox/-}$;$ROSA^{mTmG/+}$ and $Fn1^{flox/+}$; $ROSA^{mTmG/+}$ MEFs. **A.** To
858 delete Fn1, we infected $Fn1^{flox/-}$;$ROSA^{mTmG/+}$ MEFs with adenoviruses encoding Cre
859 recombinase, generating $Fn1^{\Delta/-}$ (Fn1-null) and $Fn1^{flox/-}$ (control cells). **B.** $Fn1^{flox/+}$;
860 $ROSA^{mTmG/+}$ MEFs were treated with adenoviruses encoding Cre recombinase to
861 generate control $Fn1^{\Delta/+}$ MEFs. **C.** After infection, cells were expanded and sorted.
862 Membrane-tagged GFP-expressing cells are in green, and membrane-tagged td-Tomato-
863 expressing cells are in red. **D.** Western blot using anti-Fn1 antibody shows that we
864 successfully ablated Fn1 in $Fn1^{\Delta/-}$ (Fn1-null) MEFs. β-actin was used as a loading control.
865 **E.** Densitometry quantification of Fn1 levels relative to β-actin.
866
867 **Figure S7. Monolayer scratch assay. A-D**. Cells imaged immediately after the scratch
868 wound (time=0 hrs). **A1-D1.** Cells were imaged 14 hours after the scratch (time=14 hrs).

869 White lines mark the area remaining cell-free at t=14 hours. **E**. To quantify % wound
870 closure, cell-free area at t=14 ($A_{t=14}$) was subtracted from cell-free area at t=0 ($A_{t=0}$), and
871 the % wound closure was calculated as $100*(A_{t=0} - A_{t=14})/ A_{t=0}$); n=6 independent
872 experiments. Means (horizontal bars) and standard deviations (error bars) are displayed;
873 p was calculated using a 2-tailed, unpaired Student's t-test.
874
875 **Figure S8. Deletion of Fn1 in Mesp1 lineage causes ectopic DPW differentiation**. **A-**
876 **C**. $Fn1^{flox/+}$; $Mesp1^{Cre/+}$ (Control) and **D-F** $Fn1^{flox/-}$; $Mesp1^{Cre/+}$ (Mutant) embryos were
877 dissected at E9.5 (21-26s), and stained to detect GFP (green), sarcomeric myosin heavy
878 chain (MF-20, white), and nuclei (DAPI, blue). Arrow in **E** points to cells in the aDPW
879 ectopically expressing sarcomeric myosin heavy chain. **C, F.** Ventral views of the DPW.
880 3D reconstruction of the DPW (pink) using Imaris. MF-20 staining in the DPW is marked
881 by the white surface. **G**. Schematic representation of the method used to quantify MF-20
882 staining. **H.** The length of the MF20 staining relative to the DPW length in each analyzed
883 section is plotted.Eight optical sections from 5 control and eight optical sections 8 mutant
884 embryos were analyzed. Small dots mark data from each slice; Large dots mark means.
885 Data from the same embryo is displayed with the same color. A 2-tailed, unpaired.
886 Student's t-test was used to determine p values. DPW- dorsal pericardial wall, OFT-
887 outflow tract, A- atrium. MF-20- sarcomeric myosin heavy chain.
888
889 **Figure S9. The organization of F-actin cytoskeleton in the posterior DPW does not**
890 **depend on the mesodermal Fn1. A.** $Fn1^{flox/+}$; $Mesp1^{Cre/+}$ (Control) and $Fn1^{flox/-}$;
891 $Mesp1^{Cre/+}$ (Mutant) embryos were dissected at E9.5 (21-26s), and transverse

892 cryosections (dashed line in **A**) from the middle of the DPW were stained to detect GFP
893 (green), -actin (white), and nuclei (DAPI, blue). Yellow arrows point to F-actin
894 cytoskeleton. **F-G.** Quantification of F-actin angles in the middle DPW was measured
895 relative to the apical cell side. 270 cells from 4 controls and 123 cells from 3 mutants were
896 analyzed. **H.** Percent of actin filaments oriented between 85^0 and 95^0 to the base of the
897 DPW**.** 260 cells from 4 controls and 121 cells from 3 mutants were analyzed. **I.**
898 Quantification of F-actin length in middle DPW cells. **J – M**. $Fn1^{flox/+}$; $Mesp1^{Cre/+}$ (Control)
899 and $Fn1^{flox/-}$; $Mesp1^{Cre/+}$ (Mutant) embryos were dissected at E9.5 (21-26s), and
900 transverse cryosections (dashed line in **A**) from the posterior of the DPW were stained as
901 in **B-E**. **N-O.** Quantification of F-actin angles in the posterior DPW was measured relative
902 to the apical cell side. 200 cells from 3 controls and 210 cells from 2 mutants were
903 analyzed as in **F-G**. **P.** Actin organization in cells of the posterior DPW was measured as
904 in **H**. **Q**. Quantification of F-actin length in the posterior DPW cells. Small dots mark data
905 from each cell. Large dots are means from each optical slice. Data from the same embryo
906 is displayed with the same color. Means (horizontal bars) and standard deviations (error
907 bars) are displayed; p was calculated using a 2-tailed, unpaired Student's t-test. $p<0.05$
908 is considered significant. DPW- dorsal pericardial wall, A- atrium, NT- Neural tube, OFT-
909 outflow tract, V- ventricle.

910 **Figure S10. Mesodermal Fn1 regulates DPW cell proliferation but not cell survival.**
911 **A-C.** $Fn1^{flox/+}$; $Mesp1^{Cre/+}$ (Control) and $Fn1^{flox/-}$; $Mesp1^{Cre/+}$ (Mutant) embryos were
912 dissected and stained for PHH3 (white), and nuclei (DAPI, blue). **A-B.** E8.5 (11-12s)
913 embryos. DPW (magenta) and $PHH3^+$ cells in the DPW (white) were segmented using
914 Imaris. **C**. Quantification of $PHH3^+$ cells in the DPW of E8.5 embryos, n=3 control and 4

915 mutant embryos were analyzed. **D, E, F, G.** Endoderm (orange) and PHH3$^+$ cells in the
916 endoderm (white) were segmented using Imaris. **D-E.** E8.5 embryos (11-12s) and **F-G.**
917 E9.5 embryos (20-25). **H**. Quantification of PHH3$^+$ cells in the endoderm of E8.5 embryos.
918 n=3 for each genotype. **I**. Quantification of PHH3$^+$ cells in the endoderm of E9.5 embryos
919 n=4 for each genotype. **J-J1.** Fn1$^{flox/+}$; Mesp1$^{Cre/+}$ (Control) and **K-K1.** Fn1$^{flox/-}$; Mesp1$^{Cre/+}$
920 (Mutant) embryos were dissected at E9.5 (21-26s), sectioned in the transverse
921 orientation, stained to detect GFP (green), nuclei (DAPI, blue), and apoptosis using the
922 TUNEL assay (magenta). Boxes in **J** and **K** are expanded in **J1** and **K1**. Arrows point to
923 apoptotic cells (TUNEL$^+$) in the DPW. **M.** Quantification of TUNEL$^+$ cells in the DPW. 2-
924 7 slices per embryo were analyzed. Small dots indicate the number of TUNEL$^+$ cells in
925 one slice. Large dots mark the mean in each embryo. Data from the same embryo is
926 marked with the same color. Means (horizontal bars) and standard deviations (error bars)
927 are displayed; p was calculated using a 2-tailed, unpaired Student's t-test. DPW- dorsal
928 pericardial wall, PHH3- Phosphohistone H3, TUNEL- Terminal deoxynucleotidyl
929 transferase (TdT) dUTP Nick-End Labeling.
930
931 **Figure S11. Mesodermal Fn1 regulates OFT myocardial cell proliferation at E9.5. A,**
932 **D.** Fn1$^{flox/+}$; Mesp1$^{Cre/+}$ (Control) and **B, E.** Fn1$^{flox/-}$; Mesp1$^{Cre/+}$ (Mutant) embryos were
933 dissected and stained to detect PHH3 (white) and nuclei (DAPI, blue) at E8.5 and E9.5.
934 **A-B.** E8.5 embryos (11-12s). Myocardial cells in the OFT were segmented in yellow and
935 the PHH3$^+$ cells in the OFT were segmented in white using Imaris. **D-E.** E9.5 embryos
936 (20-25s). Myocardial cells in the distal OFT were segmented in yellow, and proximal OFT
937 – in turquoise, and the PHH3+ cells in each segment were marked in white using Imaris.

938 **C, F, G.** The number of PHH3$^+$ cells was normalized for the total number of nuclei in the
939 OFT. **C**. Quantification of PHH3$^+$ cells in the OFT of E8.5 embryos. n= 3 control and 4
940 mutant embryos. **F-G**. Quantification of PHH3$^+$ cells in the distal and proximal OFT of
941 E9.5 embryos. n=4 control and 6 mutant embryos. Means (horizontal bars) and standard
942 deviations (error bars) are displayed; p was calculated using a 2-tailed, unpaired
943 Student's t-test. OFT- outflow tract, PHH3 – phosphorylated Histone H3.
944
945 **Figure S12. Deletion of mesodermal Fn1 does not alter OFT cell survival or NCC**
946 **cell migration. A-C.** Fn1$^{flox/+}$; Mesp1$^{Cre/+}$ (Control, n=3) and **D-F** Fn1$^{flox/-}$; Mesp1$^{Cre/+}$
947 (Mutant, n=3) embryos were dissected at E9.5 (21-26s), and transverse cryosections
948 were used to perform TUNEL assay (magenta), detect Mesp1 lineage by the expression
949 of GFP (green), an NCC marker TFAP2**α** (white), and nuclei (DAPI, blue). Boxes in **B** and
950 **E** are expanded in **B1, B2** and **E1, E2,** where white arrows indicate apoptotic cells
951 (magenta) in the OFT. Boxes in **C** and **F** are expanded in **C1** and **F1** where arrows point
952 to NCCs (TFAP2**α** + cells) in the PA. **G.** Quantification of the number of TUNEL$^+$ cells in
953 the OFT per section. 2 - 7 sections per embryo were analyzed. Small dots in the plots
954 mark the number of TUNEL$^+$ cells in the OFT in each section. Large dots mark the mean
955 in each embryo. **H.** Quantification of the number TFAP2**α**+ cells in the second pharyngeal
956 arch. 2 – 7 sections per embryo were analyzed. Small dots mark the number of TFAP2**α**+
957 cells in each section. Large dots mark the mean in each embryo. P was calculated using
958 a 2-tailed, unpaired Student's t-test. OFT- outflow tract, NCC cells- neural cardiac crest
959 cells, TUNEL- Terminal deoxynucleotidyl transferase (TdT) dUTP Nick-End Labeling,
960 TFAP2**α** -Transcription Factor AP-2 Alpha.

961

962 **Figure S13. Efficient downregulation of Fn1 protein in the mesoderm of Fn1$^{flox/-}$;**
963 **Mesp1$^{Cre/+}$ (Mutant) embryos. A-B2.** Fn1$^{flox/+}$; Mesp1$^{Cre/+}$ (Control) and **C-D2.** Fn1$^{flox/-}$;
964 Mesp1$^{Cre/+}$ (Mutant) embryos were dissected at E8.5 (8-12s) and stained to detect Fn1
965 protein (white) and nuclei (DAPI, blue). **E.** Ratio of Fn1 protein intensity shows similar
966 levels Fn1 in the anterior and posterior DPW embryos. **F-H.** Fn1 protein levels decrease
967 in the DPW and left ventricle in mutants. Fn1 intensity in the aDPW, pDWP and left
968 ventricle regions outlined by the red dash lines in **B1-2** and **D1-D2** was normalized by
969 DAPI intensity; 5 optical slices from 5 control and 5 mutant embryos were evaluate. **I-M.**
970 E9.5 **I-J.** Fn1$^{flox/+}$; Mesp1$^{Cre/+}$ (Control) and **K-L.** Fn1$^{flox/-}$; Mesp1$^{Cre/+}$ (Mutant) embryos
971 were dissected at E9.5 (22-26s) and stained to detect Fn1 protein (white) and nuclei
972 (DAPI, blue). Regions outlined by rectangles are expanded in **J1** and **L1**. **M**. Fn1 protein
973 expression in the left ventricle. 7 optical slices from 8 control and 10 mutant embryos were
974 evaluate. Each small dot represents one slice, and each large dot is an average of all
975 slices per embryo. Data from the same embryo is marked by the same color. Means
976 (horizontal bars) and standard deviations (error bars) are displayed, 2-tailed, unpaired
977 Student's t-test was used to determine p values. aDPW-anterior dorsal pericardial wall,
978 pDPW- posterior dorsal pericardial wall, OFT-outflow tract, A-atrium, LV-left ventricle.

979

980 **Figure S14. Fn1 synthesized by the endoderm is not required for the epithelial**
981 **organization or N-Cadherin expression in the DPW. A-C.** Fn1$^{flox/+}$ Sox17 $^{Cre/+}$ (Control)
982 and **D-F.** Fn1$^{flox/-}$ Sox17 $^{Cre/+}$ (Mutant) embryos were dissected at E9.5 (20-26s). In **A** and
983 **D,** embryos were labeled to detect *Fn1 mRNA* (turquoise). **A1** and **D1** are magnifications

984 of the DWP. White and yellow arrows indicate the mesoderm and endoderm, respectively.
985 In **B** and **E** embryos were stained to detect Fn1 protein (green), and nuclei (DAPI blue).
986 **B1** and **E1** are expanded from **B** and **E**. Arrows point to Fn1 protein staining in the DPW.
987 In **C** and **F** embryos were stained to detect N-cadherin (white). **C1** and **F1** are expanded
988 from **C** and **F.** Arrows point to N-cadherin expression at SHF cell-cell junctions in the
989 DPW. OFT- outflow tract, DPW- dorsal pericardial wall, A- atrium.

990 **Literature Cited**

991 Alfano, D., A. Altomonte, C. Cortes, M. Bilio, R.G. Kelly, and A. Baldini. 2019. Tbx1
992 regulates extracellular matrix-cell interactions in the second heart field. *Hum Mol Genet*.
993 28:2295-2308.

994 Andrews, T.G.R., W. Ponisch, E.K. Paluch, B.J. Steventon, and E. Benito-Gutierrez.
995 2021. Single-cell morphometrics reveals ancestral principles of notochord development.
996 *Development*. 148.

997 Arriagada, C., V.A. Cavieres, C. Luchsinger, A.E. Gonzalez, V.C. Munoz, J. Cancino,
998 P.V. Burgos, and G.A. Mardones. 2020. GOLPH3 Regulates EGFR in T98G
999 Glioblastoma Cells by Modulating Its Glycosylation and Ubiquitylation. *Int J Mol Sci*. 21.

1000 Bajolle, F., S. Zaffran, R.G. Kelly, J. Hadchouel, D. Bonnet, N.A. Brown, and M.E.
1001 Buckingham. 2006. Rotation of the myocardial wall of the outflow tract is implicated in
1002 the normal positioning of the great arteries. *Circ Res*. 98:421-428.

1003 Bajolle, F., S. Zaffran, S.M. Meilhac, M. Dandonneau, T. Chang, R.G. Kelly, and M.E.
1004 Buckingham. 2008. Myocardium at the base of the aorta and pulmonary trunk is
1005 prefigured in the outflow tract of the heart and in subdomains of the second heart field.
1006 *Dev Biol*. 313:25-34.

1007 Bohmer, R.M., E. Scharf, and R.K. Assoian. 1996. Cytoskeletal integrity is required
1008 throughout the mitogen stimulation phase of the cell cycle and mediates the anchorage-
1009 dependent expression of cyclin D1. *Mol Biol Cell*. 7:101-111.

1010 Borreguero-Munoz, N., G.C. Fletcher, M. Aguilar-Aragon, A. Elbediwy, Z.I. Vincent-
1011 Mistiaen, and B.J. Thompson. 2019. The Hippo pathway integrates PI3K-Akt signals
1012 with mechanical and polarity cues to control tissue growth. *PLoS Biol*. 17:e3000509.

1013 Chen, D., X. Wang, D. Liang, J. Gordon, A. Mittal, N. Manley, K. Degenhardt, and S.
1014 Astrof. 2015. Fibronectin signals through integrin alpha5beta1 to regulate
1015 cardiovascular development in a cell type-specific manner. *Dev Biol*. 407:195-210.

1016 Cortes, C., A. Francou, C. De Bono, and R.G. Kelly. 2018. Epithelial Properties of the
1017 Second Heart Field. *Circ Res*. 122:142-154.

1018 Cseh, B., S. Fernandez-Sauze, D. Grall, S. Schaub, E. Doma, and E. Van Obberghen-
1019 Schilling. 2010. Autocrine fibronectin directs matrix assembly and crosstalk between

1020 cell-matrix and cell-cell adhesion in vascular endothelial cells. *J Cell Sci*. 123:3989-
1021 3999.

1022 Dupont, S. 2016. Role of YAP/TAZ in cell-matrix adhesion-mediated signalling and
1023 mechanotransduction. *Exp Cell Res*. 343:42-53.

1024 Dzamba, B.J., K.R. Jakab, M. Marsden, M.A. Schwartz, and D.W. DeSimone. 2009.
1025 Cadherin adhesion, tissue tension, and noncanonical Wnt signaling regulate fibronectin
1026 matrix organization. *Dev Cell*. 16:421-432.

1027 Engert, S., W.P. Liao, I. Burtscher, and H. Lickert. 2009. Sox17-2A-iCre: a knock-in
1028 mouse line expressing Cre recombinase in endoderm and vascular endothelial cells.
1029 *Genesis*. 47:603-610.

1030 Fan, R., N.G. Kim, and B.M. Gumbiner. 2013. Regulation of Hippo pathway by
1031 mitogenic growth factors via phosphoinositide 3-kinase and phosphoinositide-
1032 dependent kinase-1. *Proc Natl Acad Sci U S A*. 110:2569-2574.

1033 Francou, A., C. De Bono, and R.G. Kelly. 2017. Epithelial tension in the second heart
1034 field promotes mouse heart tube elongation. *Nat Commun*. 8:14770.

1035 Francou, A., E. Saint-Michel, K. Mesbah, and R.G. Kelly. 2014. TBX1 regulates
1036 epithelial polarity and dynamic basal filopodia in the second heart field. *Development*.
1037 141:4320-4331.

1038 Friedl, P., and R. Mayor. 2017. Tuning Collective Cell Migration by Cell-Cell Junction
1039 Regulation. *Cold Spring Harb Perspect Biol*. 9.

1040 Garavito-Aguilar, Z.V., H.E. Riley, and D. Yelon. 2010. Hand2 ensures an appropriate
1041 environment for cardiac fusion by limiting Fibronectin function. *Development*. 137:3215-
1042 3220.

1043 George, E.L., H.S. Baldwin, and R.O. Hynes. 1997. Fibronectins are essential for heart
1044 and blood vessel morphogenesis but are dispensable for initial specification of
1045 precursor cells. *Blood*. 90:3073-3081.

1046 George, E.L., E.N. Georges-Labouesse, R.S. Patel-King, H. Rayburn, and R.O. Hynes.
1047 1993. Defects in mesoderm, neural tube and vascular development in mouse embryos
1048 lacking fibronectin. *Development*. 119:1079-1091.

1049 Hirsh, G.D., B.J. Dzamba, P.R. Sonavane, D.R. Shook, C.M. Allen, and D.W.
1050 DeSimone. 2018. Multiple functions for the catenin family member plakoglobin in
1051 cadherin-dependent adhesion, fibronectin matrix assembly, and *Xenopus* gastrulation
1052 movements. *bioRxiv*:318774.

1053 Kelly, R.G. 2023. The heart field transcriptional landscape at single-cell resolution. *Dev*
1054 *Cell*. 58:257-266.

1055 Kim, N.G., and B.M. Gumbiner. 2015. Adhesion to fibronectin regulates Hippo signaling
1056 via the FAK-Src-PI3K pathway. *J Cell Biol*. 210:503-515.

1057 Li, D., A. Angermeier, and J. Wang. 2019. Planar cell polarity signaling regulates
1058 polarized second heart field morphogenesis to promote both arterial and venous pole
1059 septation. *Development*. 146.

1060 Li, D., T. Sinha, R. Ajima, H.S. Seo, T.P. Yamaguchi, and J. Wang. 2016. Spatial
1061 regulation of cell cohesion by Wnt5a during second heart field progenitor deployment.
1062 *Dev Biol*. 412:18-31.

1063 Li, D., and J. Wang. 2018. Planar Cell Polarity Signaling in Mammalian Cardiac
1064 Morphogenesis. *Pediatr Cardiol*. 39:1052-1062.

1065 Luciano, M., M. Versaevel, E. Vercruysse, A. Procès, Y. Kalukula, A. Remson, A.
1066 Deridoux, and S. Gabrielea. 2022. Appreciating the role of cell shape changes in the
1067 mechanobiology of epithelial tissues. *Biophysics Reviews*. 3:011305.

1068 Marsden, M., and D.W. DeSimone. 2001. Regulation of cell polarity, radial intercalation
1069 and epiboly in Xenopus: novel roles for integrin and fibronectin. *Development*.
1070 128:3635-3647.

1071 Marsden, M., and D.W. DeSimone. 2003. Integrin-ECM interactions regulate cadherin-
1072 dependent cell adhesion and are required for convergent extension in Xenopus. *Curr*
1073 *Biol*. 13:1182-1191.

1074 Meilhac, S.M., and M.E. Buckingham. 2018. The deployment of cell lineages that form
1075 the mammalian heart. *Nat Rev Cardiol*. 15:705-724.

1076 Mittal, A., M. Pulina, S.Y. Hou, and S. Astrof. 2010. Fibronectin and integrin alpha 5 play
1077 essential roles in the development of the cardiac neural crest. *Mech Dev*. 127:472-484.

1078 Mittal, A., M. Pulina, S.Y. Hou, and S. Astrof. 2013. Fibronectin and integrin alpha 5 play
1079 requisite roles in cardiac morphogenesis. *Dev Biol*. 381:73-82.

1080 Muzumdar, M.D., B. Tasic, K. Miyamichi, L. Li, and L. Luo. 2007. A global double-
1081 fluorescent Cre reporter mouse. *Genesis*. 45:593-605.

1082 Nelson, W.J. 2003. Adaptation of core mechanisms to generate cell polarity. *Nature*.
1083 422:766-774.

1084 Nomaru, H., Y. Liu, C. De Bono, D. Righelli, A. Cirino, W. Wang, H. Song, S.E. Racedo,
1085 A.G. Dantas, L. Zhang, C.L. Cai, C. Angelini, L. Christiaen, R.G. Kelly, A. Baldini, D.
1086 Zheng, and B.E. Morrow. 2021. Single cell multi-omic analysis identifies a Tbx1-
1087 dependent multilineage primed population in murine cardiopharyngeal mesoderm. *Nat*
1088 *Commun*. 12:6645.

1089 Perez Gonzalez, N., J. Tao, N.D. Rochman, D. Vig, E. Chiu, D. Wirtz, and S.X. Sun.
1090 2018. Cell tension and mechanical regulation of cell volume. *Mol Biol Cell*. 29:0.

1091 Pulina, M.V., S.Y. Hou, A. Mittal, D. Julich, C.A. Whittaker, S.A. Holley, R.O. Hynes, and
1092 S. Astrof. 2011. Essential roles of fibronectin in the development of the left-right
1093 embryonic body plan. *Dev Biol*. 354:208-220.

1094 Ramirez, A., and S. Astrof. 2020. Visualization and Analysis of Pharyngeal Arch Arteries
1095 using Whole-mount Immunohistochemistry and 3D Reconstruction. *J Vis Exp*.

1096 Rammah, M., M. Theveniau-Ruissy, R. Sturny, F. Rochais, and R.G. Kelly. 2022.
1097 PPARgamma and NOTCH Regulate Regional Identity in the Murine Cardiac Outflow
1098 Tract. *Circ Res*. 131:842-858.

1099 Ramsbottom, S.A., V. Sharma, H.J. Rhee, L. Eley, H.M. Phillips, H.F. Rigby, C. Dean,
1100 B. Chaudhry, and D.J. Henderson. 2014. Vangl2-regulated polarisation of second heart
1101 field-derived cells is required for outflow tract lengthening during cardiac development.
1102 *PLoS Genet*. 10:e1004871.

1103 Roovers, K., and R.K. Assoian. 2003. Effects of rho kinase and actin stress fibers on
1104 sustained extracellular signal-regulated kinase activity and activation of G(1) phase
1105 cyclin-dependent kinases. *Mol Cell Biol*. 23:4283-4294.

1106 Rozario, T., B. Dzamba, G.F. Weber, L.A. Davidson, and D.W. DeSimone. 2009. The
1107 physical state of fibronectin matrix differentially regulates morphogenetic movements in
1108 vivo. *Dev Biol*. 327:386-398.

1109 Saga, Y., N. Hata, S. Kobayashi, T. Magnuson, M.F. Seldin, and M.M. Taketo. 1996.
1110 MesP1: a novel basic helix-loop-helix protein expressed in the nascent mesodermal
1111 cells during mouse gastrulation. *Development*. 122:2769-2778.

1112 Saga, Y., S. Miyagawa-Tomita, A. Takagi, S. Kitajima, J. Miyazaki, and T. Inoue. 1999.
1113 MesP1 is expressed in the heart precursor cells and required for the formation of a
1114 single heart tube. *Development*. 126:3437-3447.

1115 Sakai, T., K.J. Johnson, M. Murozono, K. Sakai, M.A. Magnuson, T. Wieloch, T.
1116 Cronberg, A. Isshiki, H.P. Erickson, and R. Fassler. 2001. Plasma fibronectin supports
1117 neuronal survival and reduces brain injury following transient focal cerebral ischemia but
1118 is not essential for skin-wound healing and hemostasis. *Nat Med*. 7:324-330.

1119 Sawyer, J.M., J.R. Harrell, G. Shemer, J. Sullivan-Brown, M. Roh-Johnson, and B.
1120 Goldstein. 2010. Apical constriction: a cell shape change that can drive morphogenesis.
1121 *Dev Biol*. 341:5-19.

1122 Singh, P., C. Carraher, and J.E. Schwarzbauer. 2010. Assembly of fibronectin
1123 extracellular matrix. *Annu Rev Cell Dev Biol*. 26:397-419.

1124 Sinha, T., D. Li, M. Theveniau-Ruissy, M.R. Hutson, R.G. Kelly, and J. Wang. 2015.
1125 Loss of Wnt5a disrupts second heart field cell deployment and may contribute to OFT
1126 malformations in DiGeorge syndrome. *Hum Mol Genet*. 24:1704-1716.

1127 Sinha, T., B. Wang, S. Evans, A. Wynshaw-Boris, and J. Wang. 2012. Disheveled
1128 mediated planar cell polarity signaling is required in the second heart field lineage for
1129 outflow tract morphogenesis. *Dev Biol*. 370:135-144.

1130 Soh, B.S., K. Buac, H. Xu, E. Li, S.Y. Ng, H. Wu, J. Chmielowiec, X. Jiang, L. Bu, R.A.
1131 Li, C. Cowan, and K.R. Chien. 2014. N-cadherin prevents the premature differentiation
1132 of anterior heart field progenitors in the pharyngeal mesodermal microenvironment. *Cell*
1133 *Res*. 24:1420-1432.

1134 Somlyo, A.P., and A.V. Somlyo. 1994. Signal transduction and regulation in smooth
1135 muscle. *Nature*. 372:231-236.

1136 Stefanovic, S., B. Laforest, J.P. Desvignes, F. Lescroart, L. Argiro, C. Maurel-Zaffran, D.
1137 Salgado, E. Plaindoux, C. De Bono, K. Pazur, M. Theveniau-Ruissy, C. Beroud, M.
1138 Puceat, A. Gavalas, R.G. Kelly, and S. Zaffran. 2020. Hox-dependent coordination of
1139 mouse cardiac progenitor cell patterning and differentiation. *Elife*. 9.

1140 Theveniau-Ruissy, M., M. Dandonneau, K. Mesbah, O. Ghez, M.G. Mattei, L. Miquerol,
1141 and R.G. Kelly. 2008. The del22q11.2 candidate gene Tbx1 controls regional outflow
1142 tract identity and coronary artery patterning. *Circ Res*. 103:142-148.

1143 Trinh, L.A., and D.Y. Stainier. 2004. Fibronectin regulates epithelial organization during
1144 myocardial migration in zebrafish. *Dev Cell*. 6:371-382.

1145 Trinh, L.A., D. Yelon, and D.Y. Stainier. 2005. Hand2 regulates epithelial formation
1146 during myocardial diferentiation. *Curr Biol*. 15:441-446.

1147 Tsao, C.W., A.W. Aday, Z.I. Almarzooq, A. Alonso, A.Z. Beaton, M.S. Bittencourt, A.K.
1148 Boehme, A.E. Buxton, A.P. Carson, Y. Commodore-Mensah, M.S.V. Elkind, K.R.
1149 Evenson, C. Eze-Nliam, J.F. Ferguson, G. Generoso, J.E. Ho, R. Kalani, S.S. Khan,
1150 B.M. Kissela, K.L. Knutson, D.A. Levine, T.T. Lewis, J. Liu, M.S. Loop, J. Ma, M.E.
1151 Mussolino, S.D. Navaneethan, A.M. Perak, R. Poudel, M. Rezk-Hanna, G.A. Roth, E.B.
1152 Schroeder, S.H. Shah, E.L. Thacker, L.B. VanWagner, S.S. Virani, J.H. Voecks, N.Y.
1153 Wang, K. Yaffe, S.S. Martin, E. American Heart Association Council on, C. Prevention
1154 Statistics, and S. Stroke Statistics. 2022. Heart Disease and Stroke Statistics-2022
1155 Update: A Report From the American Heart Association.
1156 *Circulation*:CIR0000000000001052.

1157 Turner, C.J., K. Badu-Nkansah, and R.O. Hynes. 2017. Endothelium-derived fibronectin
1158 regulates neonatal vascular morphogenesis in an autocrine fashion. *Angiogenesis*.
1159 20:519-531.

1160 Walker, J.L., A.K. Fournier, and R.K. Assoian. 2005. Regulation of growth factor
1161 signaling and cell cycle progression by cell adhesion and adhesion-dependent changes
1162 in cellular tension. *Cytokine Growth Factor Rev*. 16:395-405.

1163 Wang, X., and S. Astrof. 2016. Neural crest cell-autonomous roles of fibronectin in
1164 cardiovascular development. *Development*. 143:88-100.

1165 Weber, G.F., M.A. Bjerke, and D.W. DeSimone. 2011. Integrins and cadherins join
1166 forces to form adhesive networks. *J Cell Sci*. 124:1183-1193.

1167 Xia, M., W. Luo, H. Jin, and Z. Yang. 2019. HAND2-mediated epithelial maintenance
1168 and integrity in cardiac outflow tract morphogenesis. *Development*. 146.

1169 Zhang, Q., D. Carlin, F. Zhu, P. Cattaneo, T. Ideker, S.M. Evans, J. Bloomekatz, and
1170 N.C. Chi. 2021. Unveiling Complexity and Multipotentiality of Early Heart Fields. *Circ*
1171 *Res*. 129:474-487.

1172 Zimmerman, S.P., S.B. Asokan, B. Kuhlman, and J.E. Bear. 2017. Cells lay their own
1173 tracks - optogenetic Cdc42 activation stimulates fibronectin deposition supporting
1174 directed migration. *J Cell Sci*. 130:2971-2983.
1175

Figure 1

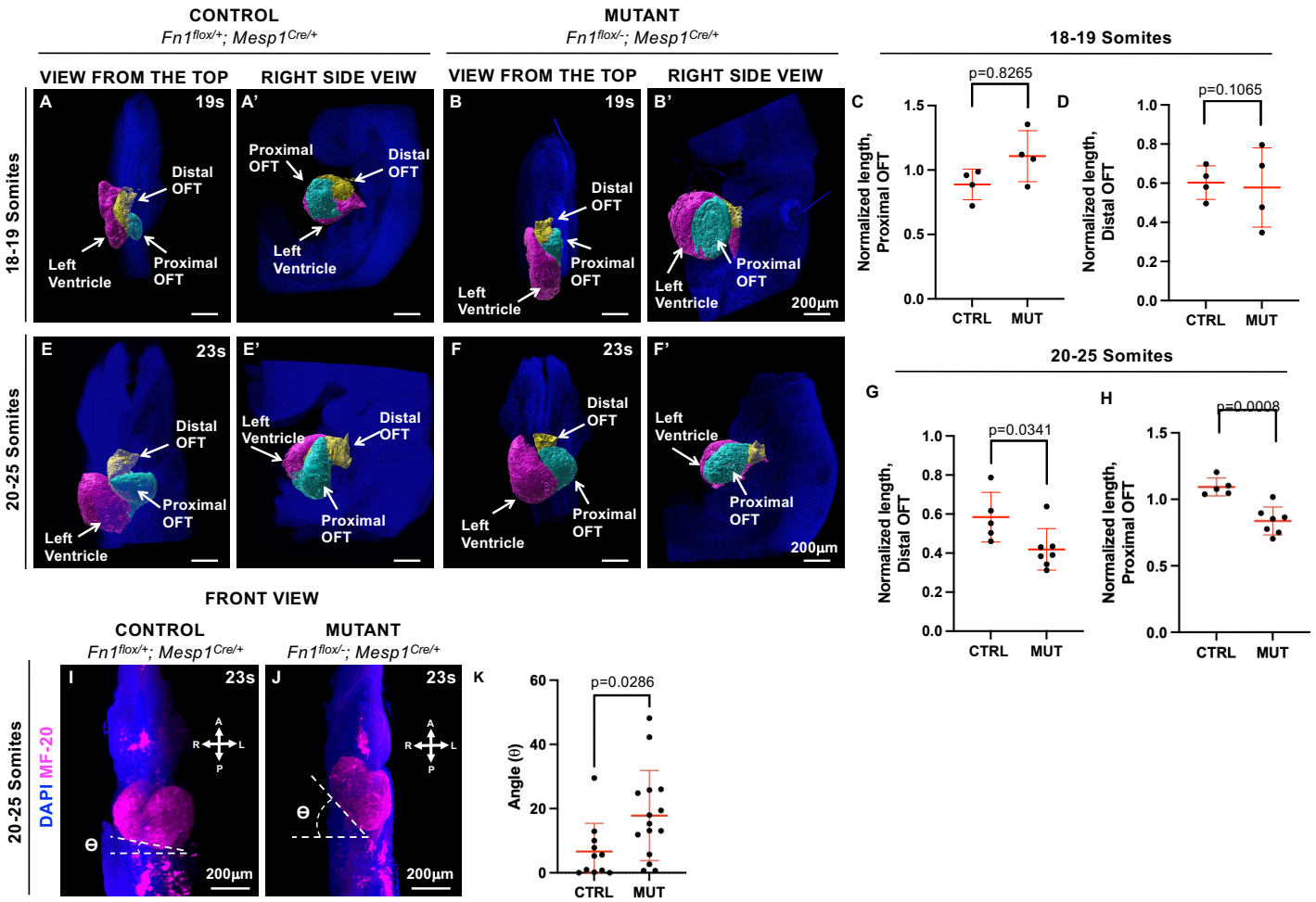

Figure 1. The expression of Fn1 in Mesp1 lineage is required for the OFT elongation.

Fn1$^{flox/+}$; Mesp1$^{Cre/+}$ (Control) and Fn1$^{flox/-}$; Mesp1$^{Cre/+}$ (Mutant) embryos were dissected at E9.5 and staged according to somite number. **A-D.** Embryos between 18-19 somites. n=5 controls and 4 mutants. **E-H.** Embryos between 20-25 somites, n= 5 control and 7 mutant embryos. Imaris was used to surface distal OFT (yellow), proximal OFT (turquoise), and the left ventricle and atria (pink)**. C-D, G-H.** The length of the distal and proximal OFT in each embryo was normalized to the height of the left ventricle to control for embryo size.

I-J. Fn1$^{flox/+}$; Mesp1$^{Cre/+}$ (Control) and Fn1$^{flox/-}$; Mesp1$^{Cre/+}$ (Mutant) embryos were dissected at E9.5 (20-25s) and stained with DAPI and the MF-20 antibody. **K**. Quantification of angles in controls and mutants as shown in **I-J**. n= 9 controls and 13 mutants. Means (horizontal bars) and standard deviations (error bars) are displayed; p was calculated using a 2-tailed, unpaired Student's t-test. OFT-outflow tract, MF-20- antibody detects sarcomeric myosin heavy chain. All scale bars : 200 µm

Figure 2

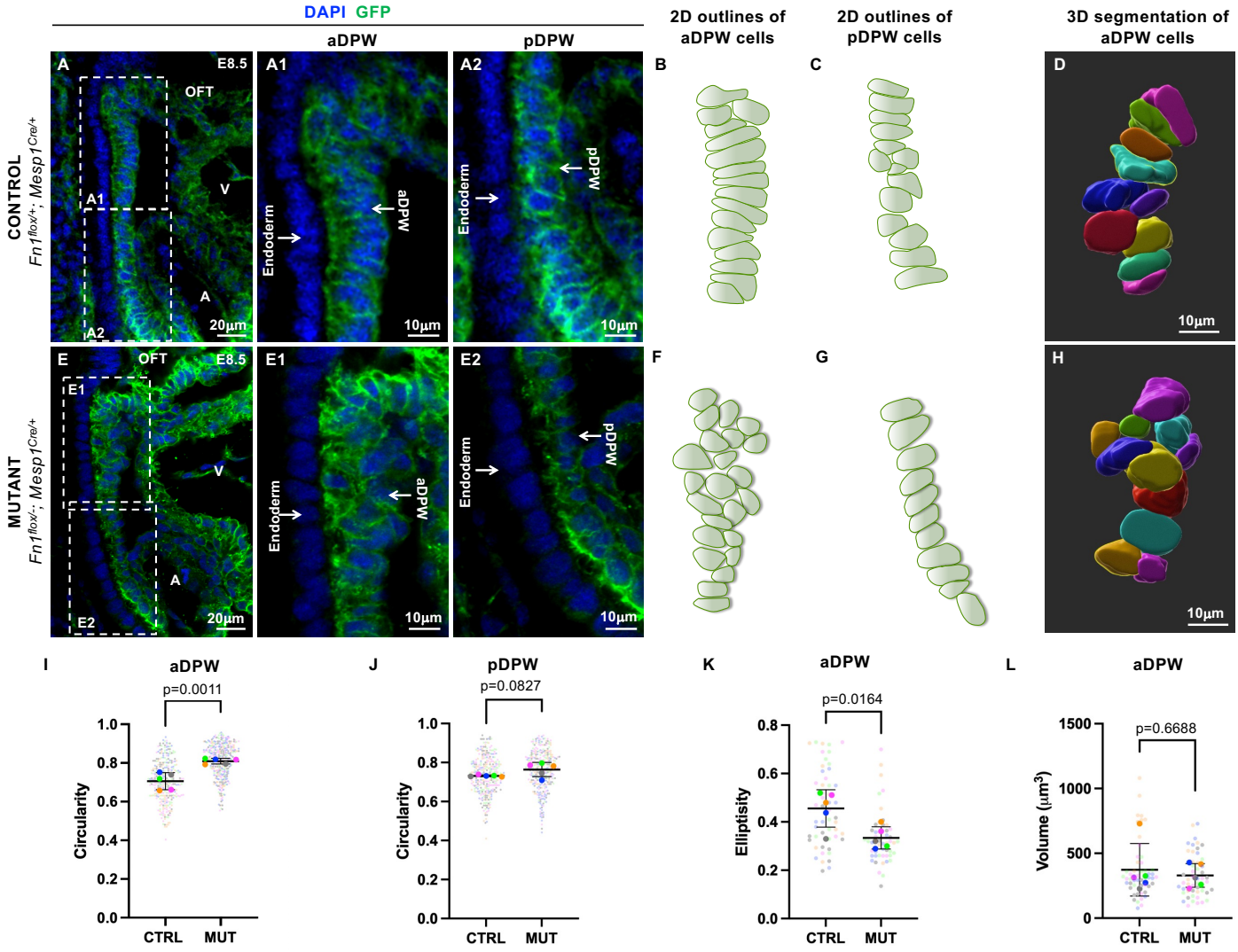

Figure 2. The expression of Fn1 in the mesoderm is important for the regulation of cell shape in the anterior DPW at E8.5. **A.** Fn1$^{flox/+}$; Mesp1$^{Cre/+}$ (Control) and **E.** Fn1$^{flox/-}$; Mesp1$^{Cre/+}$ (Mutant) embryos were dissected at E8.5 (9-11s) and stained to detect GFP (green) and nuclei (DAPI, blue). Regions marked by dashed rectangles in **A, B** are magnified in **A1-E1** and **A2-E2**. **B-C, F-G.** Outlines of aDPW and pDPW cells. **D** and **H.** 3D reconstruction of aDPW cells. **I-L.** Cell shape analyses. Small dots mark data points from each cell; large dots mark the average per embryo. Data points from one embryo are marked with the same color. **I-J**. Cell circularity. **I.** 320 cells from 5 control and 367 cells from 5 mutant embryos were analyzed. **J.** 311 cells from 5 control and 326 cells from 5 mutant embryos were analyzed. **K-L.** Ellipticity and volume of aDPW cells; 51 cells from 5 control and 50 cells from mutant embryos were analyzed. Means (horizontal bars) and standard deviations (error bars) are displayed; p was calculated using a 2-tailed, unpaired Student's t-test. OFT-outflow tract, aDPW-anterior dorsal pericardial wall, pDPW-posterior dorsal pericardial wall, A-atrium, V-ventricle

Figure 3

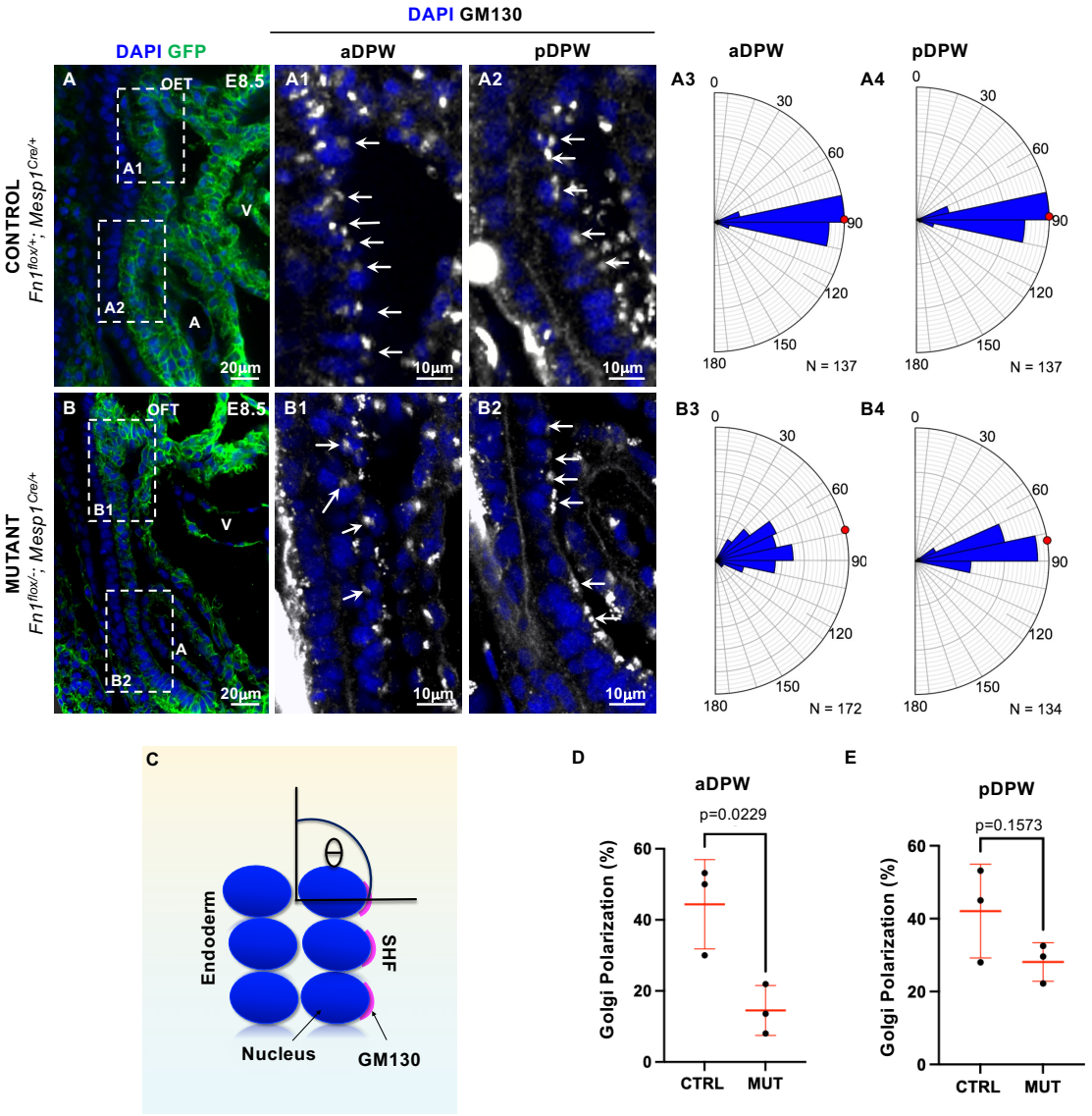

Figure 3. Expression of Fn1 in the mesoderm regulates Golgi apparatus orientation in the anterior DPW. A-A2. Fn1$^{flox/+}$; Mesp1$^{Cre/+}$ (Control) and **B-B2.** Fn1$^{flox/-}$; Mesp1$^{Cre/+}$ (Mutant) embryos were dissected at E8.5 (9-11s) and stained to detect GFP (green), GM130 (white), and nuclei (DAPI, blue). Boxes in **A, B** are magnified in the panels to the right. Arrows point to Golgi. **A3, A4, B3, B4.** Semicircular histograms represent the distribution of the Golgi orientation angles in SHF cells that were measured as is indicated in **C** . N=total number of cells analyzed in 3 controls and 3 mutants. **D, E.** Quantification of Golgi polarization. Golgi was considered polarized if the angle between the Golgi and the plane of the endoderm fell between 85^0 and 95^0. OFT-outflow tract, aDPW-anterior dorsal pericardial wall, pDPW-posterior dorsal pericardial wall, A-atrium, V-ventricle.

Figure 4

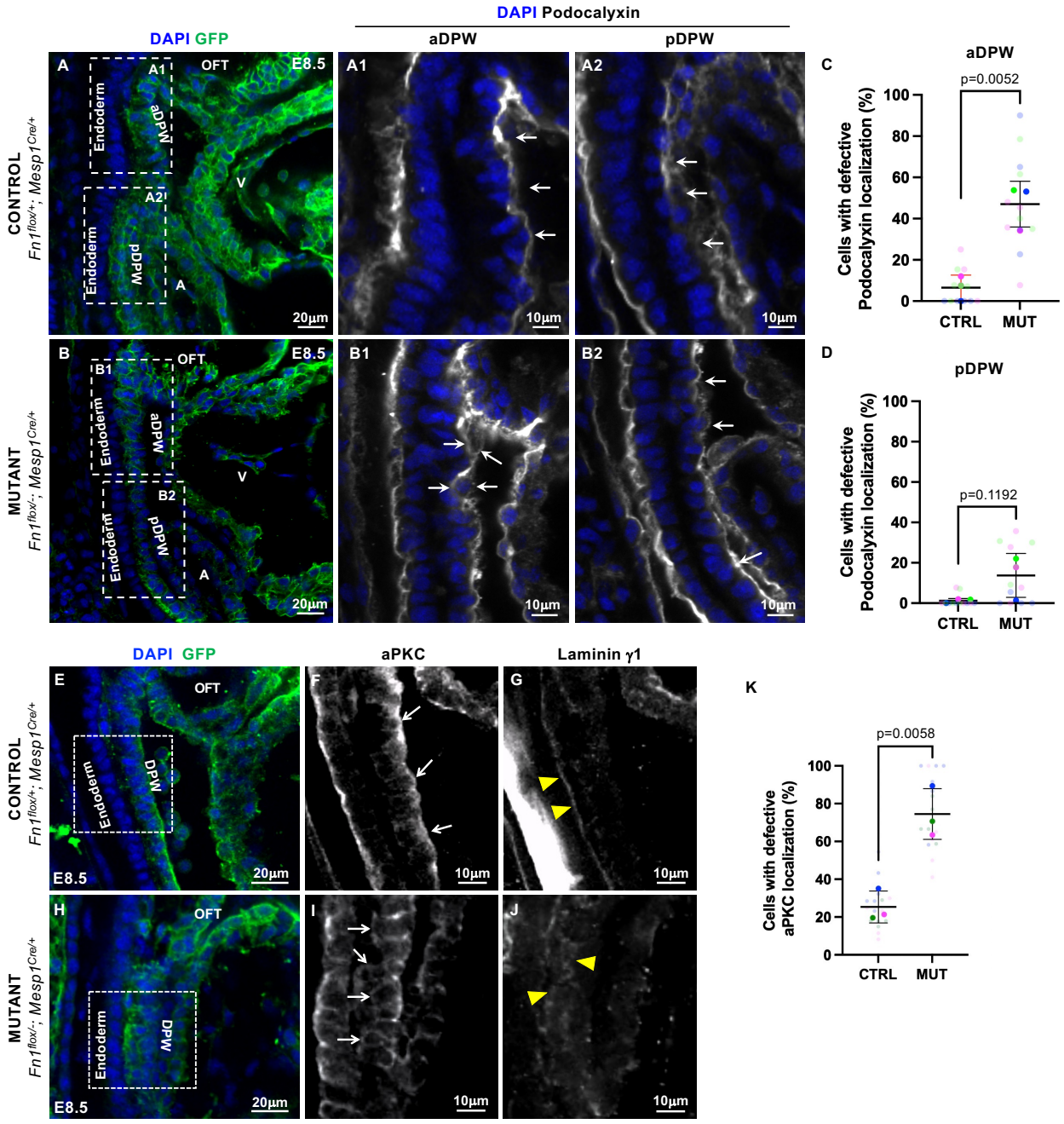

Figure 4. Expression of Fn1 in the mesoderm regulates cell polarity in the anterior DPW. A. Fn1$^{flox/+}$; Mesp1$^{Cre/+}$ (Control) and **B.** Fn1$^{flox/-}$; Mesp1$^{Cre/+}$ (Mutant) embryos were dissected at E8.5 (9-11s), and stained to detect GFP (green), podocalyxin (white), and nuclei (DAPI, blue). Boxes in **A** and **B** were expanded in **A1** and **B1** to show the anterior DPW and in **A2** and **B2** to show the posterior DPW. Arrows in **A1** point to cells with apical localization of podocalyxin. Arrows in **B1** point to defective basolateral localization of podocalyxin in mutants. **A2, B2.** Podocalyxin is localized apically in the posterior DPW, arrows. **C-D** Quantification of cells with defective podocalyxin localization in the anterior and posterior DPW. **C.** 148 cells in the aDPW from 3 controls and 224 cells in aDPW from 3 mutants were analyzed. **D.** 149 cells in the pDPW from 3 controls and 182 cells in the pDPW from 3 mutants were analyzed. Each small dot represents data from one slice, and each large dot is an average of all slices per embryo. Data from the same embryo is marked by the same color. **E-G.** Fn1$^{flox/+}$; Mesp1$^{Cre/+}$ (Control) and **H-J.** Fn1$^{flox/-}$; Mesp1$^{Cre/+}$ (Mutant) embryos were dissected at E8.5 (7-8s), and stained for GFP (green), aPKC, laminin γ1, and nuclei (DAPI, blue). Arrows in **F** point to apical localization of aPKC in control DPW cells. **I.** Arrows point to defective basolateral localization of aPKC in mutants. Arrowheads in **G** point to basal localization of laminin γ1 in controls and in **J** to disorganized localization of laminin γ1 in one of three mutants. **K.** Quantification of cells in which aPKC was re-distributed away from the apical surface. DPW cells from 5 different slices were evaluated in 3 control and 3 mutant embryos. Each small dot represents data from one slice, and each large dot is an average of all slices per embryo. Data from the same embryo is marked by the same color. Means (horizontal bars) and standard deviations (error bars) are displayed; p was calculated using a 2-tailed, unpaired Student's t-test. OFT-outflow tract, aDPW-anterior dorsal pericardial wall, pDPW-posterior dorsal pericardial wall, A-atrium, V-ventricle.

Figure 5

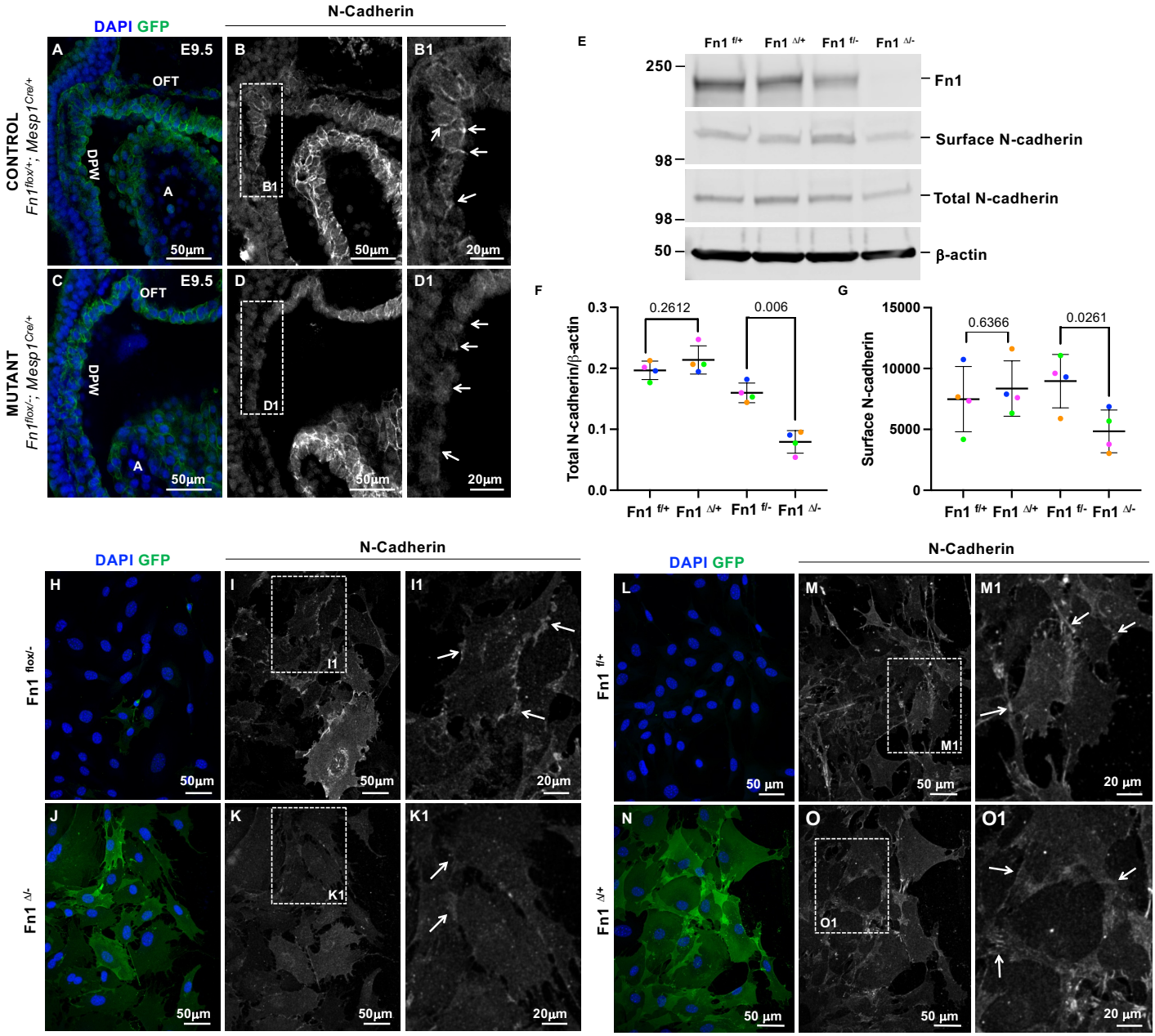

Figure 5. Mesodermal Fn1 regulates the expression of N-Cadherin at cell-cell junctions in the DPW. A-B. $Fn1^{flox/+}$; $Mesp1^{Cre/+}$ (Control) and **C-D.** $Fn1^{flox/-}$; $Mesp1^{Cre/+}$ (Mutant) embryos were dissected at E9.5 (21-26s) and stained to detect GFP (green), N-cadherin (white) and nuclei (DAPI, blue). Junctional N-Cadherin is enriched in the anterior DPW (boxed region in **B**). Boxes in **B-D** are expanded in **B1 and D1.** Arrows point to DPW. **E.** Western blot analysis of total cell lysates and cell surface proteins. Positions of molecular weight markers are indicated on the left. **F-G**. Densitometrical quantification of immunoblot signals. N = 4 for each genotype. Each experiment is represented by a dot of a different color. Means (horizontal bars) and standard deviations (error bars) are displayed, and a 2-tailed, unpaired Student's t-test was used to determine p values. **H-K.** Immunostaining to detect GFP (green), N-cadherin (white) and nuclei (DAPI, blue) in $Fn1^{flox/-}$, $Fn1^{\Delta/-}$ (Fn1-null), $Fn1^{flox/+}$, and $Fn1^{\Delta/+}$ MEFs. Boxes in **I-K** and in **M-O** are expanded in **I1-K1 and M1-O1.** Arrows point to N-cadherin at cell junctions in control MEFs (**I1, M1, and O1**) and to the absent N-cadherin in Fn1-null MEFs (**K1**). DPW- dorsal pericardial wall, OFT-outflow tract, A-atrium.

Figure 6

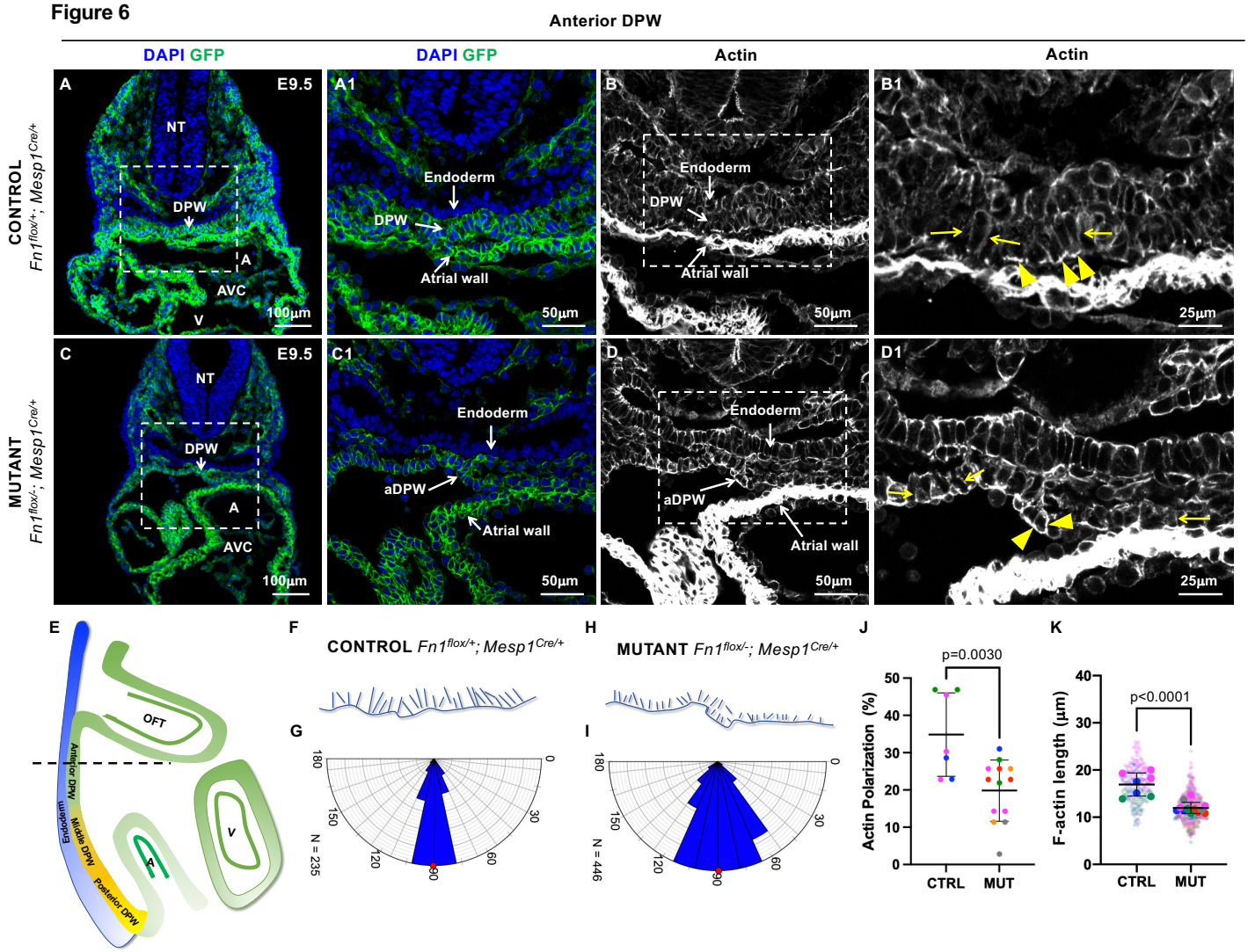

Figure 6. Mesodermal Fn1 regulates the length and organization of F-actin in the anterior DPW. A-B1. Fn1$^{flox/+}$; Mesp1$^{Cre/+}$ (Control) and **C-D1.** Fn1$^{flox/-}$; Mesp1$^{Cre/+}$ (Mutant) embryos were dissected at E9.5 (21-26s), and transverse cryosections (a plain of sections shown by the dashed line in **E**) from the anterior DPW were stained to detect GFP (green), F-actin (white), and nuclei (DAPI, blue). Yellow arrows point to F-actin in the aDPW in **B1** and **D1**. Yellow arrowheads point to apically enriched F-actin in B1 and re-distributed F-actin in **D1**. **E.** Schematic representation of the different regions in the DPW. **F-H.** Traces of F-actin in control and mutants. **G-I.** Angles made by F-actin filaments relative to cells' apical surface were measured. **J.** Quantification of actin polarization. An actin filament was considered polarized if was between 85 and 95 degrees relative to the apical surface of the DPW. **K** Quantification of the F-actin length in the anterior DPW; 235 cells from 3 controls and 417 cells from 5 mutants were examined. Small dots mark the F-actin length of individual cells, and large dots mark the average per slice. Dots from the same embryo are displayed in the same color. Means (horizontal bars) and standard deviations (error bars) are displayed; p was calculated using a 2-tailed, unpaired Student's t-test. DPW-dorsal pericardial wall, A-atrium, NT-Neural tube, AVC-atrioventricular canal, OFT-outflow tract, V-ventricle.

Figure 7

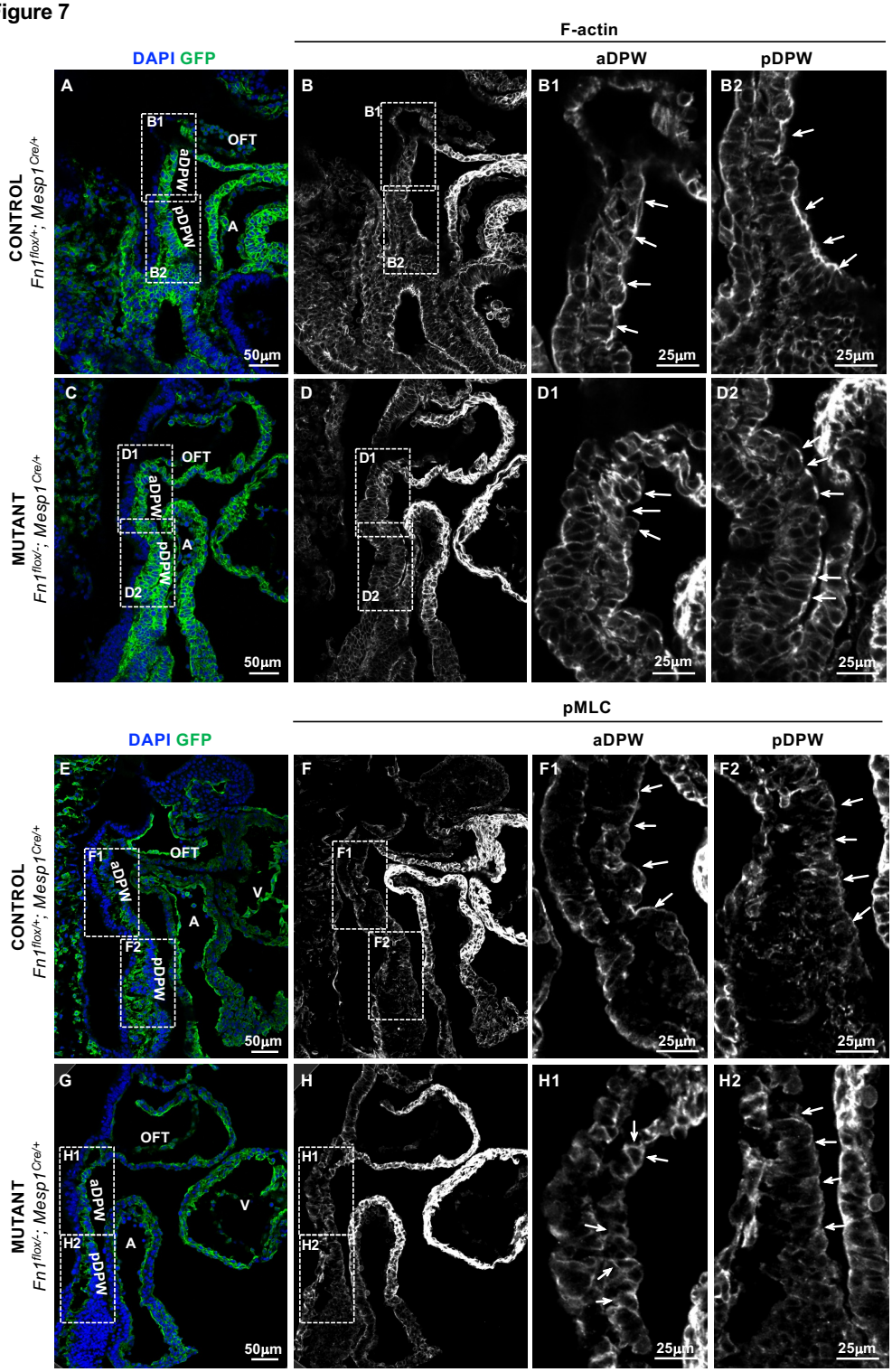

Figure 7 Mesodermal Fn1 regulates the expression of pMLC in the anterior DPW. A-B2. Fn1$^{flox/+}$; Mesp1$^{Cre/+}$ (Control) and **C-D.** Fn1$^{flox/-}$; Mesp1$^{Cre/+}$ (Mutant) embryos were dissected at E9.5 (21-26s), and sagittal cryosections were stained to detect GFP (green), F-actin (white) and nuclei (DAPI, blue). Boxes in **A-B** were expanded in **B1** and **B2** to show the anterior and posterior DPW, respectively. Boxes in **C-D** were expanded, in **D1** and **D2**, to show the anterior and posterior DPW, respectively. Arrows point to the apical enrichment of F-actin in the anterior and posterior of controls and to the lack of such enrichment in the anterior DPW of the mutants (**D1**). 6 controls and 3 mutants were analyzed. **E-H2.** Fn1$^{flox/+}$; Mesp1$^{Cre/+}$ (Control) and **C-D.** Fn1$^{flox/-}$; Mesp1$^{Cre/+}$ (Mutant) embryos were dissected at E9.5 (21-26s) and sagittal cryosections were stained to detect GFP (green), pMLC (white) and nuclei (DAPI, blue). Boxes in **E-F** are expanded in **F1** and **F2** to show the anterior and posterior DPW, respectively. Boxes in **G-H** are expanded in **H1** and **H2** to show anterior and posterior DPW, respectively. Arrows in **F1** indicate cells with apical localization of pMLC. Arrows in **H1** show a defective basolateral localization of pMLC in mutants. **F2, H2.** pMLC is localized apically in the posterior DPW. 8 controls and 3 mutants were analyzed.

Figure 8

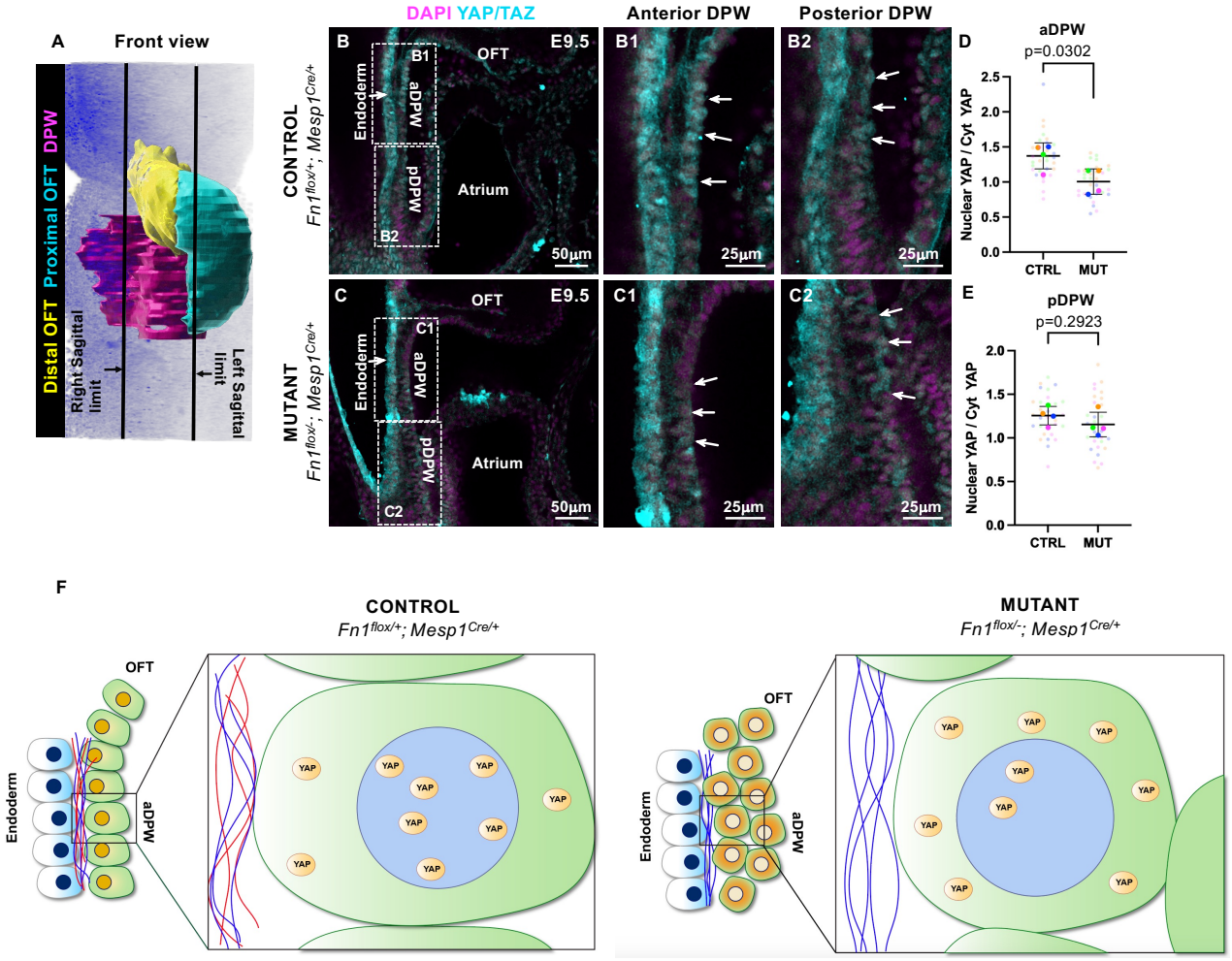

Figure 8. Mesodermal Fn1 regulates nuclear localization of YAP. A. Ventral view of E9.5 embryo. YAP localization was assayed in the DPW between the left and the right limits (marked by the vertical lines).

B-B2. Fn1$^{flox/+}$; Mesp1$^{Cre/+}$ (Control) and **C-C2.** Fn1$^{flox/-}$; Mesp1$^{Cre/+}$ (Mutant) embryos were dissected at E9.5 (23-26s) and stained to detect nuclei (DAPI, magenta) and YAP (cyan). Regions outlined by dashed rectangles are expanded in **B1, C1** (anterior DPW) and **B2, C2** (posterior DPW). **D-E**. Quantification of the intensity ratio between nuclear and cytosolic YAP in the aDPW and pDPW. 7-8 optical slices from 4 controls and 7-8 optical slices from 4 mutant embryos were analyzed. Each small dot represents one slice, and each large dot is an average of all slices in one embryo. Data from the same embryo is marked by the same color. **F.** Summary: YAP is enriched in the nuclei in the presence of both the mesodermal (red lines) and endodermal (blue lines) Fn1. In the absence of mesodermal Fn1, nuclear translocation of YAP are decreased. aDPW- anterior dorsal pericardial wall, pDPW-posterior dorsal pericardial wall, OFT-outflow tract.

Figure 9

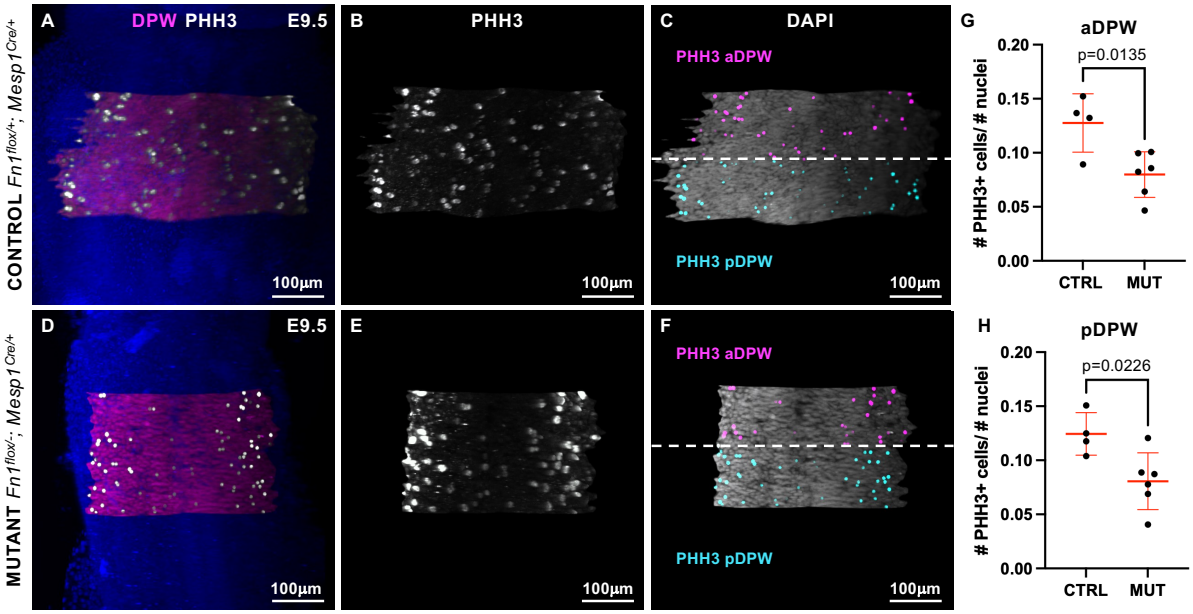

Figure 9. Mesodermal Fn1 is required for DPW cell proliferation. A-C. Fn1$^{flox/+}$; Mesp1$^{Cre/+}$ (Control) and **D-F** Fn1$^{flox/-}$; Mesp1$^{Cre/+}$ (Mutant) embryos were dissected at E9.5 (20-25s) and stained for PHH3 (white), and nuclei (DAPI, blue) E9.5 (20-25s). **A,B, D, E**. DPW (magenta) and PHH3^{+} cells in the DPW (white) were segmented using Imaris. **C,F**. Proportion of PHH3+ cells in the aDPW (magenta) and pDPW (turquoise) were quantified in **G-H**. Each dot marks one embryos. n=4 control and 6 mutant embryos. Means (horizontal bars) and standard deviations (error bars) are displayed, 2-tailed, unpaired Student's t test was used to determine p values. aDPW-anterior dorsal pericardial wall, pDPW- posterior dorsal pericardial wall, PHH3- Phosphorylated Histone H3.

Figure 10

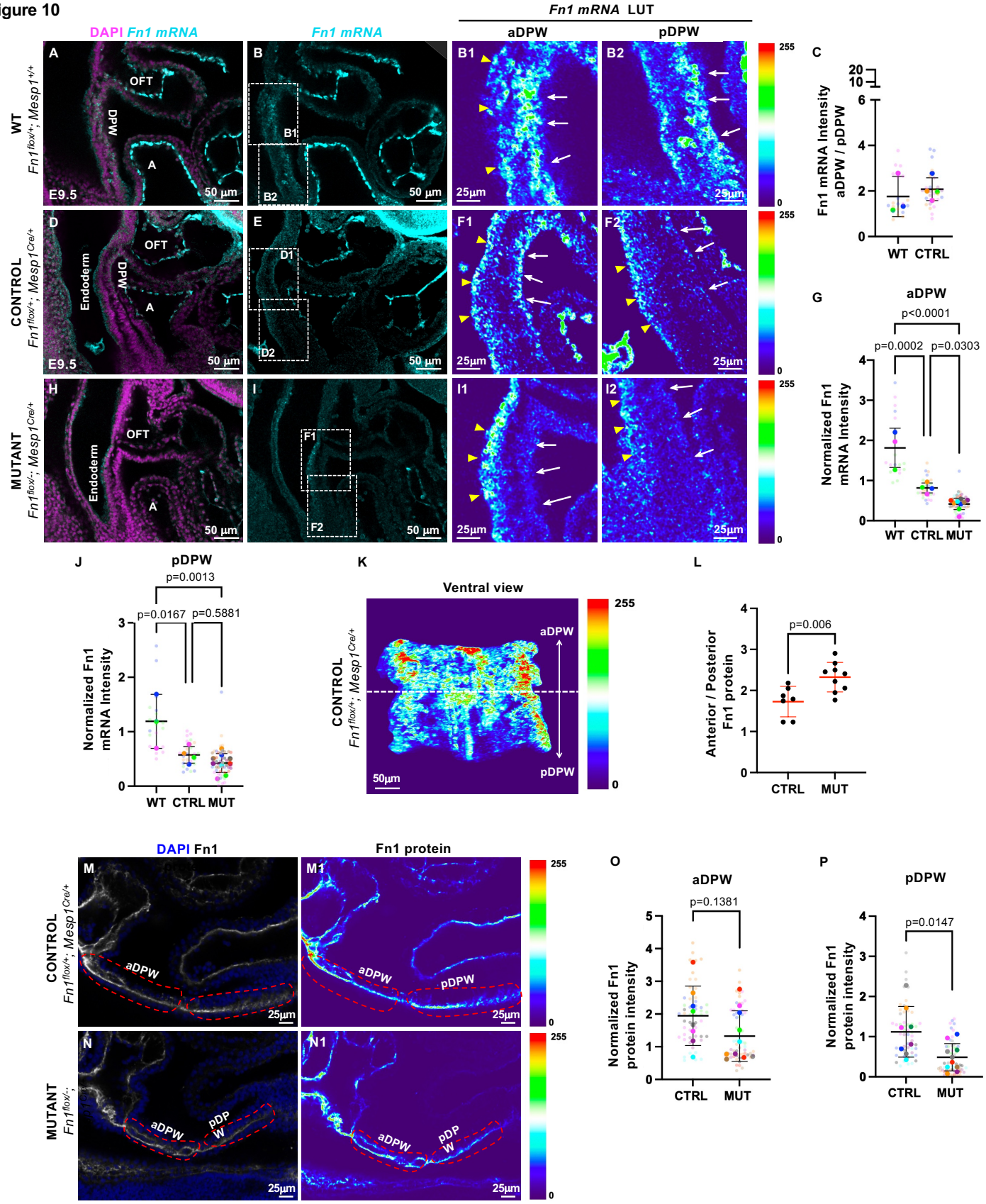
Fn1 mRNA LUT
DAPI Fn1 mRNA
Fn1 mRNA
aDPW
pDPW
WT
Fn1flox/+; Mesp1+/+
CONTROL
Fn1flox/+; Mesp1Cre/+
MUTANT
Fn1flox/-; Mesp1Cre/+
OFT
DPW
Endoderm
A
E9.5
50 µm
25µm
255
0
Fn1 mRNA Intensity aDPW / pDPW
WT CTRL
Normalized Fn1 mRNA Intensity
p<0.0001
p=0.0002
p=0.0303
WT CTRL MUT
p=0.0013
p=0.0167
p=0.5881
Ventral view
50µm
Anterior / Posterior Fn1 protein
p=0.006
CTRL MUT
DAPI Fn1
Fn1 protein
Normalized Fn1 protein intensity
p=0.1381
p=0.0147

Figure 10. Expression patterns of *Fn1 mRNA* and protein in controls and mutants. **A-J.** Expression of *Fn1 mRNA*. Embryos were dissected at E9.5 (23-26s) and labeled with DAPI (magenta) and anti-sense Fn1 probe (turquoise). **A-B2** $Fn1^{flox/+}$; $Mesp1^{+/+}$ (designated as WT), **C.** *Fn1 mRNA* intensity ratio between aDPW and pDPW, **D-F2.** $Fn1^{flox/+}$; $Mesp1^{Cre/+}$ (Control) **G.** *Fn1 mRNA* intensity in the anterior (**H**) and posterior (**J**) DPW was normalized to that in the endoderm. 6 different slices from 3 WT, 4 control and 9 mutant embryos were analyzed. **H-I2.** $Fn1^{flox/-}$;$Mesp1^{Cre/+}$ (Mutant) embryos. Regions outlined by the dotted rectangles in **B, E,** and **I** are expanded in panels to the right and color-coded according to fluorescence intensity (scale is on the right). White arrows point to DPW. Yellow arrowheads point to the endoderm. **K.** Ventral view of the DPW, Fn1 expression is color-coded according to fluorescence intensity. **L.** Ratio of Fn1 protein intensity shows similar enrichment of Fn1 in the anterior DPW of controls and mutants. **M, M1.** $Fn1^{flox/+}$; $Mesp1^{Cre/+}$ (Control) and **N, N1.** $Fn1^{flox/-}$; $Mesp1^{Cre/+}$ (Mutant) embryos were dissected at E9.5 (22-26s) and stained to detect Fn1 protein (white) and nuclei (DAPI, blue). Fn1 protein expression in the DPW (**M, N**) is color-coded according to fluorescence intensity in **M1, N1**. **O-P.** Fn1 protein levels underlying the anterior DPW are unchanged in the mutants. Fn1 intensity in the aDPW and pDWP regions outlined by the red dash lines in **M1-N1** was normalized by DAPI intensity; 7 optical slices from 8 control and 10 mutant embryos were evaluated. Each small dot represents one slice, and each large dot is an average of all slices per embryo. Data from the same embryo is marked by the same color. Means (horizontal bars) and standard deviations (error bars) are displayed, 2-tailed, unpaired Student's t-test was used to determine p values. aDPW-anterior dorsal pericardial wall, pDPW-posterior dorsal pericardial wall, OFT-outflow tract, A-atrium, LV-left ventricle.

Figure 11

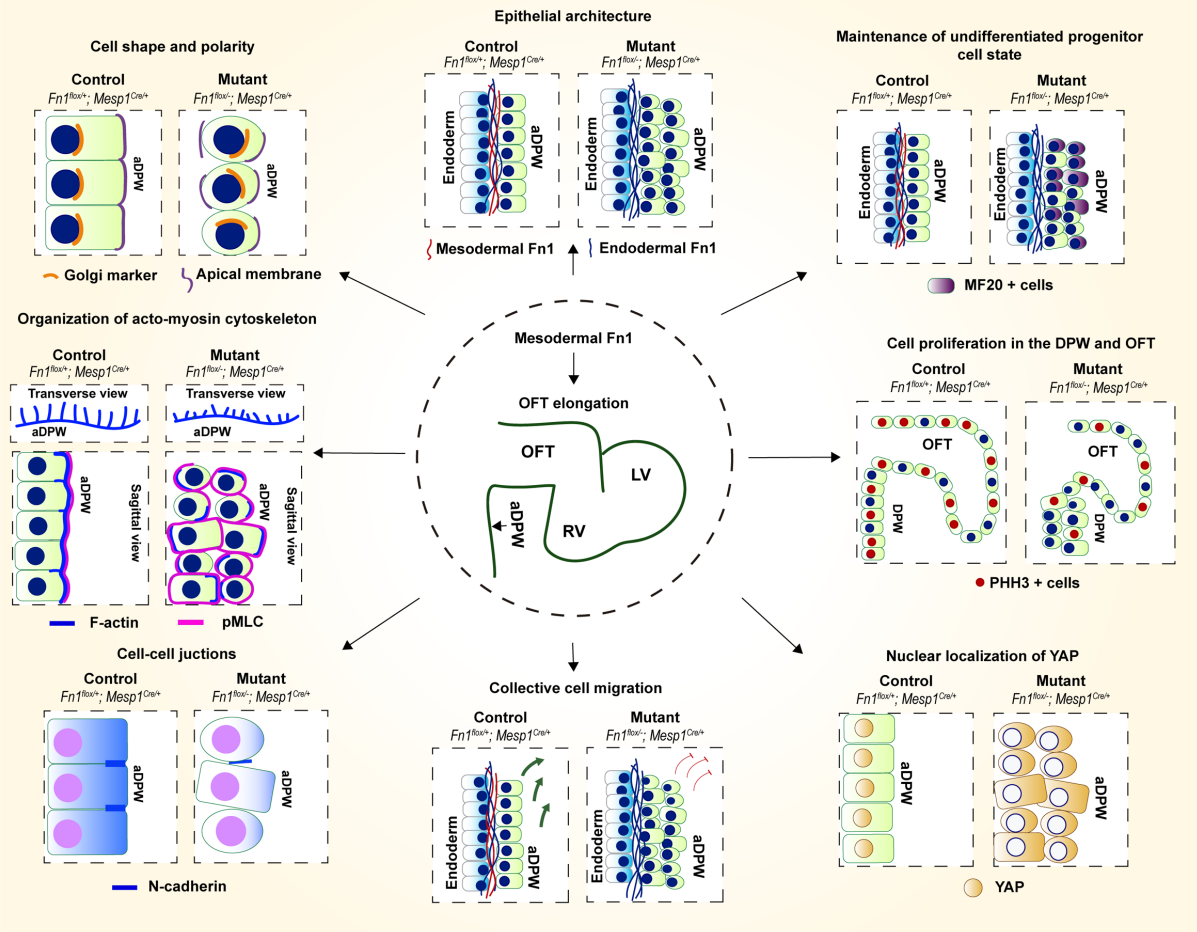

Figure 11. The central role of the mesodermal Fn1 in regulating the elongation of the cardiac outflow tract. Fn1 synthesized by the mesoderm mediates the elongation of the cardiac outflow tract by regulating cell shape, polarity, proliferation, and mechanotransduction in the anterior dorsal pericardial wall (aDPW).